## General Disclaimer

## One or more of the Following Statements may affect this Document

- This document has been reproduced from the best copy furnished by the organizational source. It is being released in the interest of making available as much information as possible.

- This document may contain data, which exceeds the sheet parameters. It was furnished in this condition by the organizational source and is the best copy available.

- This document may contain tone-on-tone or color graphs, charts and/or pictures, which have been reproduced in black and white.

- This document is paginated as submitted by the original source.

- Portions of this document are not fully legible due to the historical nature of some of the material. However, it is the best reproduction available from the original submission.

NATIONAL AERONAUTICS AND SPACE ADMINISTRATION

*Technical Report 32-1417*

# *Radio Frequency Performance of a 210-ft Ground Antenna: X-Band*

*D. A. Bathker*





JET PROPULSION LABORATORY
CALIFORNIA INSTITUTE OF TECHNOLOGY
PASADENA, CALIFORNIA

December 15, 1969

07

NATIONAL AERONAUTICS AND SPACE ADMINISTRATION

*Technical Report 32-1417*

# *Radio Frequency Performance of a 210-ft Ground Antenna: X-Band*

*D. A. Bathker*

**JET PROPULSION LABORATORY**
**CALIFORNIA INSTITUTE OF TECHNOLOGY**
**PASADENA, CALIFORNIA**
December 15, 1969

## Preface

The work described in this report was performed by the Telecommunications Division of the Jet Propulsion Laboratory.

## Acknowledgment

The advanced antenna system X-band evaluation program produced definitive results because of the efforts of many individuals. R. Stevens and G. Levy originally suggested the program. Dr. A. Moffett of the California Institute of Technology advised on source selection and possible improvements in radiometric technique.

C. Stelzried, B. Seidel, and T. Otoshi provided the noise instrumentation, data reduction software, and important feedcone calibrations. F. Gricher's extended support of the feedcone ground operational checkouts led to smooth performance on the antenna. Preparations by D. Girdner and the Servo Group of the Mars Deep Space Station for precision antenna pointing and manipulations provided outstanding operational performance. K. Bartos, R. Cormack, D. Neff, B. Seidel, and H. Reilly, Jr., contributed to the operational tests for long hours. M. Inouye and R. Norman efficiently handled the machine-reduced data.

Special comments for the structural engineers are in order. Without briefings by S. Katow, K. Bartos, and C. Valencia on structural predictions and measurements, the operational tests would have occupied far longer than the five days available. Many of S. Katow's analytic structural results are incorporated in this report for full coverage of this most important area.

Finally mention must be made of the superb 24-hour-a-day operations support by members of the Bendix Field Engineering Corporation teams at the Venus and Mars Deep Space Stations.

## Contents



## Tables

## Contents (contd)

### Figures

## Abstract

The 85- and 210-ft paraboloidal ground antennas of the Deep Space Instrumentation Facility, operated by the Jet Propulsion Laboratory for the National Aeronautics and Space Administration, have previously been demonstrated to operate well below gain limit at S-band. An 85-ft structure was recently evaluated at X-band and found to remain below gain limit. The results of an abbreviated appraisal of the radio frequency performance of the Goldstone 210-ft advanced antenna system at X-band show that in the good weather conditions encountered the aperture efficiency was in outstanding agreement with predictions. Both the surface tolerance of the reflecting system and the precision of the pointing system were found adequate for X-band. It is concluded that a significant ground capability for weather-dependent space communications or radio or radar astronomy is available at X-band with this instrument.

# Radio Frequency Performance of a 210-ft Ground Antenna: X-Band

## I. Introduction

The Deep Space Instrumentation Facility (DSIF) 210-ft-diameter advanced antenna system (AAS) was placed in operation at Goldstone, California, early in 1966. Initial radio frequency (RF) tests at S-band, 2295 MHz, were conducted using *Surveyor I* spacecraft signals from the lunar surface. These tests firmly established certain characteristics of the far-field radiation patterns (Ref. 1) as well as the aperture efficiency (Ref. 2). The wavefront loss, caused by imperfections in the reflecting surfaces, was very small and therefore poorly resolved with the S-band wavelength. Both the precision and accuracy of the pointing system were found entirely adequate to support S-band deep space tracking with straightforward ephemeris command. The initial RF feed equipment used and noise temperature performance obtained are given elsewhere (Refs. 3 and 4).

The construction of a listen-only feed for X-band, 8448 MHz, was begun late in 1966. Described in detail in Ref. 5, the X-band cassegrain experimental (XCE) feedcone is interchangeable among DSIF 85- and 210-ft reflectors. By the use of an excellent collimation tower at one of the Goldstone 85-ft stations, that station was calibrated at X-band by precision ground-based techniques (Ref. 5). Later observation of the radio source Cygnus A (3C405) during 1967 fulfilled a primary goal of obtaining a calibrated celestial source at X-band for the 210-ft X-band evaluation. A secondary goal of proving operating procedures, exercising hardware and software, and gaining further confidence in performance predictions was accomplished.

This report is divided into two sections. The predicted performance of the AAS at X-band including the important surface tolerance effects will be discussed, followed by the measured RF results obtained during February 1968.

## II. Predicted Performance of the AAS: X-Band

### A. Radio Frequency Optics Efficiency

The RF optics efficiency of the AAS fed with the XCE feedcone system was evaluated by describing the primary feed patterns (Fig. 1) and the subreflector configuration (Fig. 2) as input to the Rusch scattering program (Ref. 6).

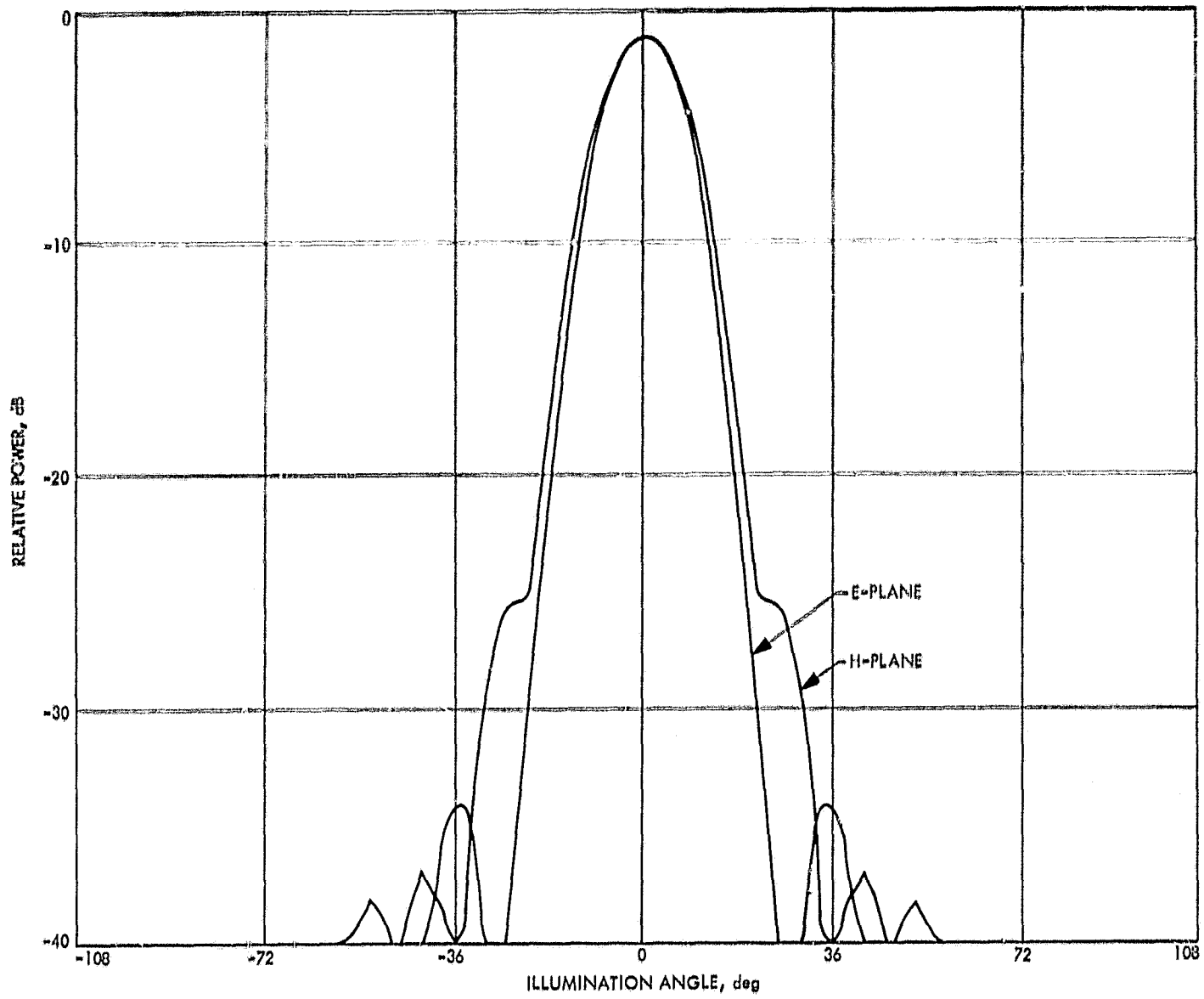


**Fig. 1. Primary feed radiation patterns**

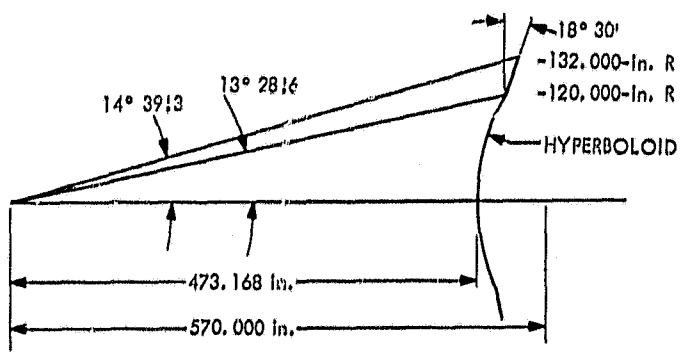


**Fig. 2. Subreflector configuration**

The scattered patterns shown in Figs. 3 and 4 illustrate distortion occurring near the edge of the paraboloid (illumination angle 50–60 deg) caused by the optimum S-band beam shaping flange. As with the earlier 85-ft-diameter antenna evaluation at X-band, the removal of the S-band flange was not considered necessary. The scattered patterns were then evaluated with the techniques of Ludwig (Ref. 7). Results of this procedure are summarized in Table 1 for a hypothetical dissipationless feed illuminating a perfect reflector without quadripod. The tolerance noted is an estimated $1\sigma$ value.

**Table 1. Feed efficiency of the XCE feedcone**

| Description | Value, % |
|---|---|
| Component | |
| Forward spillover | 99.22 |
| Rear spillover | 0.20 |
| Illumination efficiency | 86.81 |
| Cross-polarization efficiency | 99.94 |
| Phase efficiency | 96.62 |
| Subreflector blocking efficiency | 96.45 |
| Overall feed efficiency | 74.86 ± 0.20 |

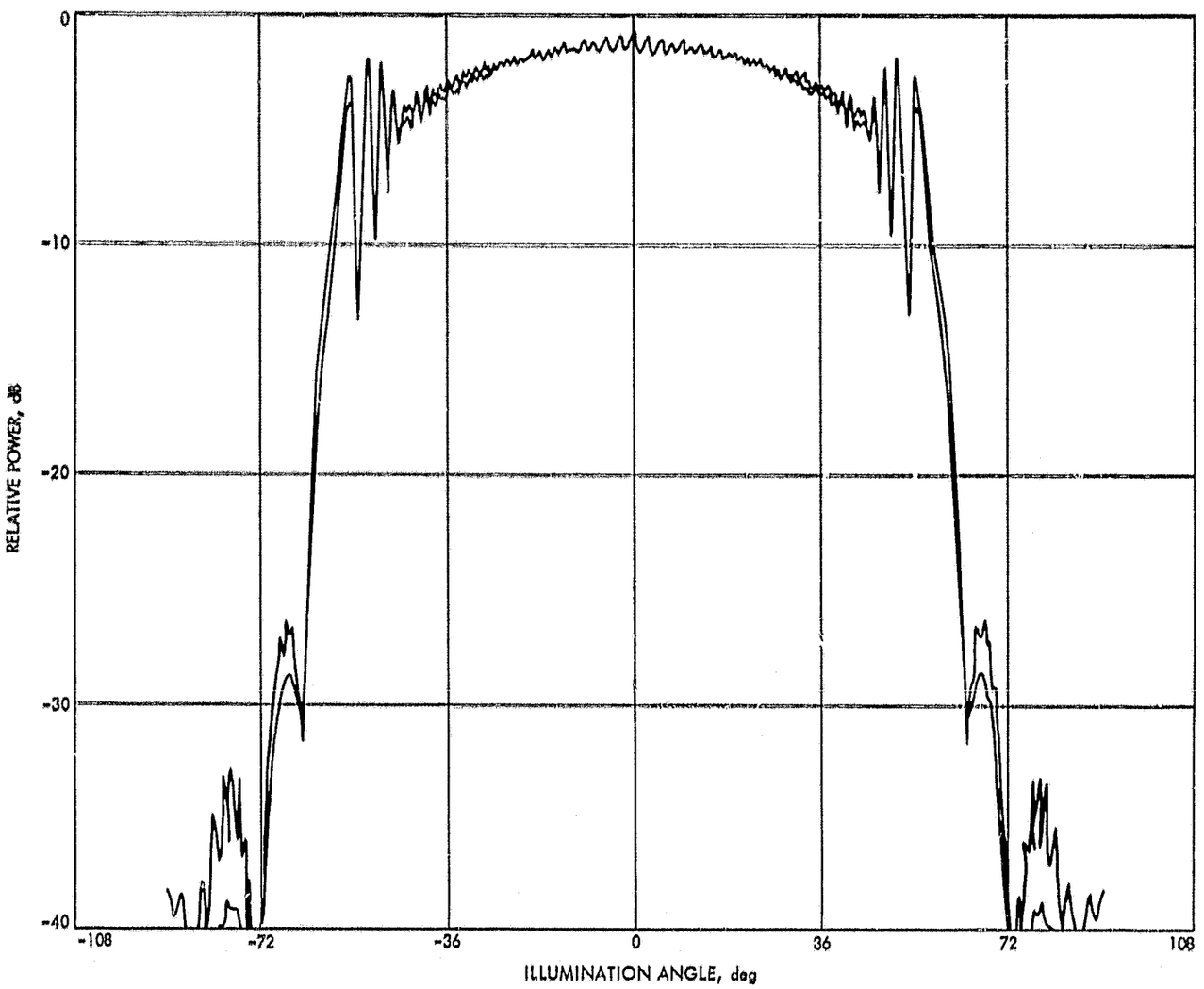


**Fig. 3. Subreflector scattered radiation patterns, amplitude**

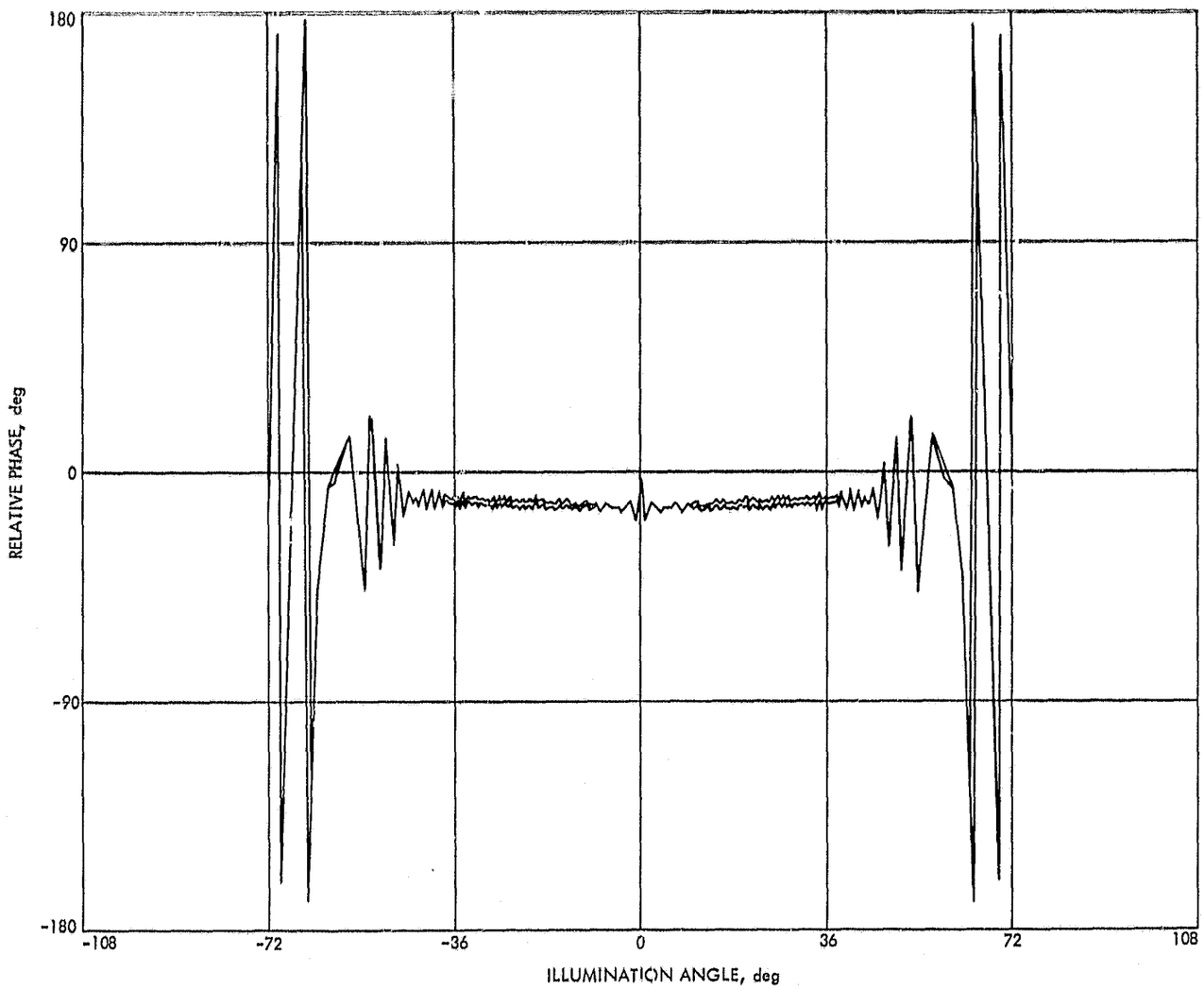


**Fig. 4. Subreflector scattered radiation patterns, phase**

An optical analysis of the AAS quadripod, an illuminated model of which is shown in Fig. 5, reveals that the structure blocks 6.255% of the available aperture. Assuming that the percentage of intercepted energy equals the percentage of area, which constitutes accepting "pie-slice" approximations of the blocked areas in the aperture, it has been shown (Ref. 5) that

$$\frac{\eta'}{\eta} = (1 - B)^2$$

where $\eta'/\eta$ is the blocking efficiency, and $B$ is the fractional area blocked. Actually $B = \sigma A$ where $A$ is the optically blocked area and $\sigma$ is defined as an average RF opacity. Because of the large wavelength size of the quadripod cross section at X-band, the opacity is estimated as $0.8 < \sigma < 1.2$. Table 2 gives the components considered and the overall quadripod blocking efficiency, again with an estimated $1\sigma$ tolerance.

**Table 2. Quadripod efficiency of the 210-ft antenna**

| Description | Value, % |
|---|---|
| Component | |
| Blocked area $A$ | 6.255 |
| Opacity $\sigma$ | 80–120 |
| Overall quadripod blocking efficiency $\eta'/\eta$ | 87.88 ± 2.4 |

The dissipative attenuation between the antenna reference flange and the maser reference flange was previously measured as 0.150 dB ± 0.0018 dB, $3\sigma$. Estimates of polarizer and feedhorn losses are 0.025 and 0.018 dB, respectively. Table 3 gives the components considered and the overall waveguide efficiency with an estimated $1\sigma$ tolerance.

**Table 3. Waveguide efficiency of the XCE feedcone**

| Description | Attenuation, dB |
|---|---|
| Component | |
| Antenna to maser flanges | 0.150 ± 0.002 |
| Turnstile junction | 0.025 ± 0.025 |
| Feedhorn | 0.018 ± 0.018 |
| Overall waveguide efficiency, 95.65 ± 0.22% | |

The final value for the RF optics efficiency of the AAS fed with the XCE feedcone system may be obtained from Tables 1, 2, and 3 as

$$\eta_0 = 0.629 \pm 0.024$$

where the tolerance quoted is again an estimated $1\sigma$ value, primarily because of quadripod blocking uncertainty.

### B. Surface Tolerance Characteristics

The methods used to analytically obtain the distortions of the 210-ft-antenna reflectors under gravity loading have been described by Kat[illegible] Ref. 8 and are here summarized in the interests of [illegible]eness and clarity. A clear understanding of the [illegible]e tolerance of the system is considered necessary to [illegible]lize the ultimate performance limitations of the instrument at short wavelengths.

Gravity deflections from the STAIR structural computing program were evaluated by use of the RMS program (Ref. 9). The RMS program yields the root mean square of one-half the RF pathlengths of the residuals, following best-fitting to a perfect paraboloid. The perfect paraboloid is free to assume a new focal length as one of the fitting parameters. The root mean square so computed represents the distortions occurring in the backup structure, or panel support points, only.

Because the AAS surface panels are aligned when the structure is oriented to a 45-deg elevation angle, only panel manufacturing and setting errors are present when at this attitude. Table 4 gives the measured distortions, the total of which has been considered a constant noise-like perturbation to be added to the gravity and other distortions at other attitudes.

**Table 4. Measured surface distortion of the 210-ft antenna at 45-deg elevation angle**

| Description | Distortion, rms in. |
|---|---|
| Component | |
| Surface-panel setting | 0.019 |
| Primary surface-panel manufacturing | 0.035 |
| Subreflector manufacturing | 0.027 |
| Total ½ RF-pathlength distortion | 0.048 |

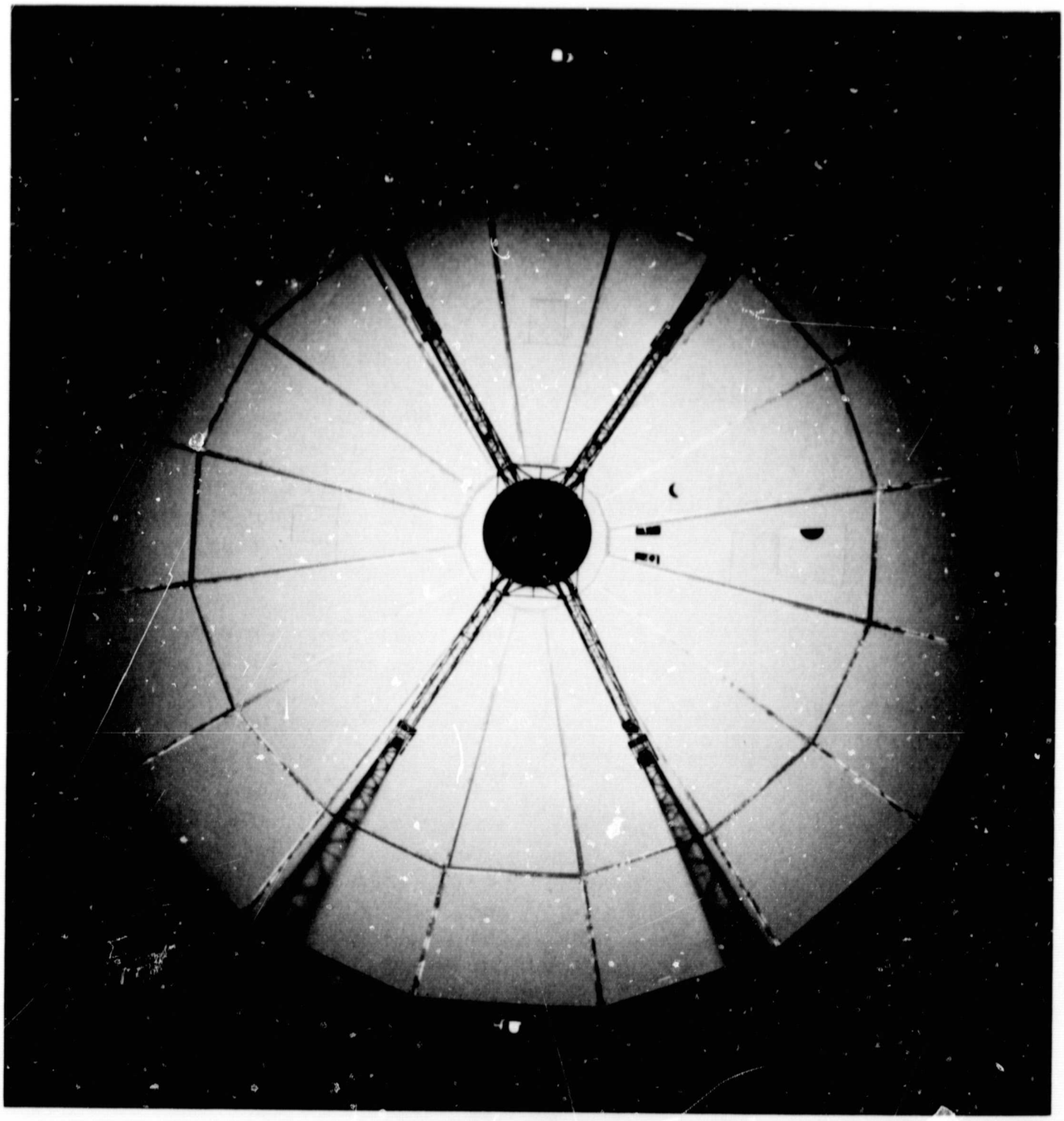

Fig. 5. Model of 210-ft-antenna quadripod

The primary result of Katow's work is summarized in Table 5 (Ref. 8). Table 5 shows that the STAIR and RMS programs were applied in 15-deg elevation angle increments. Best-fit paraboloid translations and $x$-axis rotation are noted as well as quadripod and subreflector deflections. The 45-deg elevation angle alignment procedure is seen in Table 5 to result in an absence of gravity distortions. The second part of Table 5 shows the effect of lateral and axial misalignments of the RF feed focus, considered to be tightly coupled to the subreflector–feedhorn system, from the best-fit paraboloid focus, expressed in rms equivalent error. Figure 6, which shows the rms equivalent error caused by axial and lateral misalignments, was obtained from studies conducted with the JPL radiation pattern programs which numerically evaluate the scalar far-field radiation pattern integral (Refs. 10 and 11). In the second part of Table 5, note again the absence of gravity effects at 45-deg elevation until the final summations. The power sum of the 4 key components (each expressed in rms inches)—the lateral and axial misalignments occurring at the paraboloid focus, the paraboloid structure gravity distortion, and the noise-like component previously mentioned—is finally taken in two ways. The first sum allows for axial focusing of the subreflector, and the second constrains the system to a fixed-focus mode. The fixed-focus mode had previously been adopted for S-band operations. Figure 7, after the work of Ruze (Ref. 12), relates rms surface tolerance to surface tolerance efficiency for the wavelength of interest. From Fig. 7 and Table 5 it is clear that the improvement available by axial focusing is worth the effort at X-band.

**Table 5. Computed surface distortions of the 210-ft antenna from change in direction of gravity vector from 45-deg elevation (Ref. 8)**

| Source | Elevation angle, deg | | | | | | |
|---|---|---|---|---|---|---|---|
| | 0 | 15 | 30 | 45 | 60 | 75 | 90 |
| Best-fit paraboloid data | | | | | | | |
| Vertex $y$-coordinate, in. | 1.588 | 1.403 | 0.806 | 0.0 | −1.121 | −2.426 | −3.829 |
| Vertex $z$-coordinate, in. | 0.070 | 0.044 | 0.021 | 0.0 | −0.016 | −0.026 | −0.029 |
| Rotation $x$-axis, rad | 0.001015 | 0.000894 | 0.000548 | 0.0 | −0.000712 | −0.001539 | −0.002427 |
| Focal length change, in. | −0.693 | −0.439 | −0.203 | 0.0 | 0.156 | 0.253 | 0.285 |
| Quadripod apex $z$-deflection, in. | −0.025 | −0.015 | −0.009 | 0.0 | 0.004 | 0.007 | 0.010 |
| Subreflector $z$-deflection, in. | −0.048 | −0.028 | −0.017 | 0.0 | 0.004 | 0.007 | 0.010 |
| Axial-indicated position, in. | −0.77 | −0.48 | −0.22 | 0.0 | 0.16 | 0.27 | 0.31 |
| Lateral $y$-direction deflection, in. | −1.1 | −0.5 | −0.1 | 0.0 | 0.9 | 1.8 | 2.8 |
| Subreflector | | | | | | | |
| Lateral offset equivalent error, rms. in. | 0.019 | 0.008 | 0.001 | 0.0 | 0.015 | 0.031 | 0.050 |
| Axial offset equivalent error, rms in. | 0.058 | 0.036 | 0.017 | 0.0 | 0.012 | 0.020 | 0.023 |
| Best-fit paraboloid reflector structure distortion from 45-deg, rms in. | 0.040 | 0.032 | 0.018 | 0.0 | 0.023 | 0.048 | 0.075 |
| 45-deg ½ RF-pathlength,[a] rms in. | 0.048 | 0.048 | 0.048 | 0.048 | 0.048 | 0.048 | 0.048 |
| Total ½ RF-pathlength distortion—focused axially, rms in. | 0.065 | 0.058 | 0.051 | 0.048 | 0.055 | 0.075 | 0.102 |
| Total ½ RF-pathlength distortion—focused only at 45-deg, rms in. | 0.085 | 0.068 | 0.054 | 0.048 | 0.057 | 0.077 | 0.105 |

[a]Field-measured distortion from Table 4.

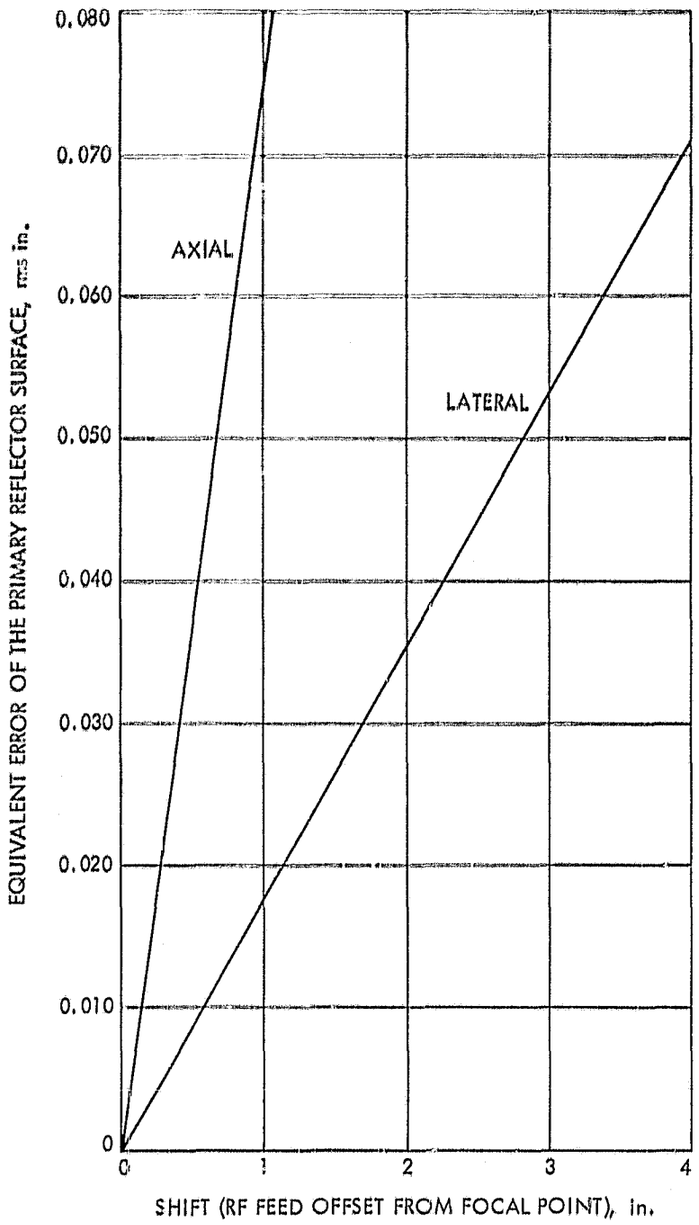


**Fig. 6. Equivalent root-mean-square error as a function of feedpoint axial and lateral shifts for 210-ft antenna**

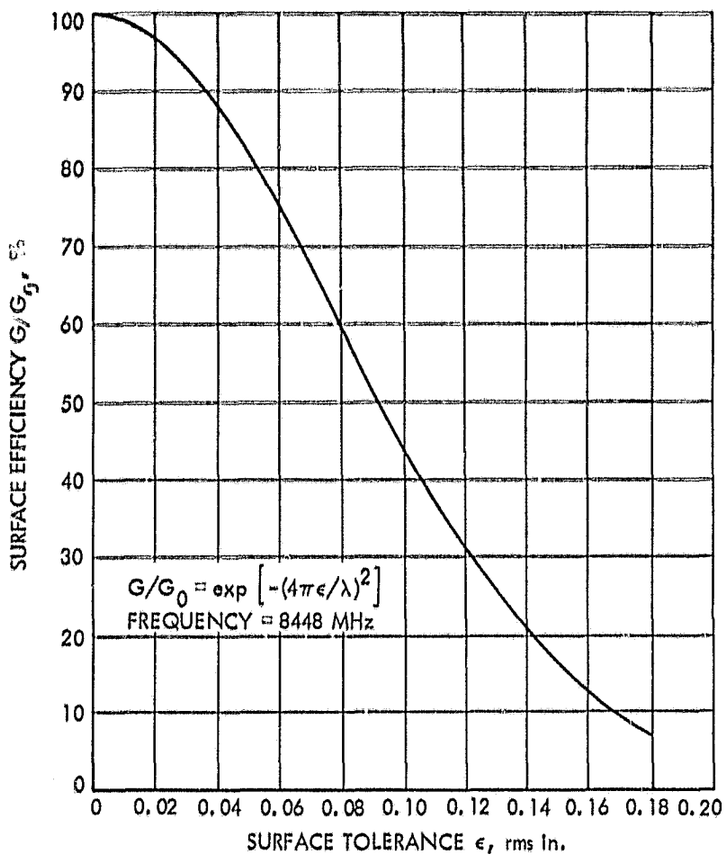


**Fig. 7. Surface efficiency as a function of surface tolerance**

Computer-organized contour plots of the horizon and zenith attitude distortions, expressed in one-half the RF pathlength to the best-fit paraboloid, are given in Figs. 8 and 9. Also shown are the field measurements that were obtained through careful application of the tape and theodolite civil engineering technique. In both cases the field measurements approximate 85% of the analytic computations, for the best-fit paraboloid structure component. As shown in Table 6, when the system is at the zenith attitude the field-measured data suggest a slightly better system (0.094 rms in.) than the computer (0.102 rms in.). When at the horizon attitude, the system is negligibly different between the field-measured data and the computed.

The structural computations were based on a uniformly illuminated paraboloid. No specific study of a possible discrepancy between results obtained here and results obtained from some form of feed amplitude weighting is available. This possible discrepancy is considered small. Also, as described in Ref. 8, the tipping structure of the

**Table 6. Field-measured surface distortion of 210-ft antenna at 0- and 90-deg elevation angle**

| Source | Distortion, rms in. | |
|---|---|---|
| | 0 deg | 90 deg |
| Component | | |
| 45-deg elevation ½ RF-pathlength distortion | 0.048 | 0.048 |
| Reflector structure gravity deflections from 45-deg elevation | 0.034 | 0.063 |
| Subreflector lateral offset | 0.020 | 0.050 |
| Total ½ RF-pathlength distortion | 0.062 | 0.094 |

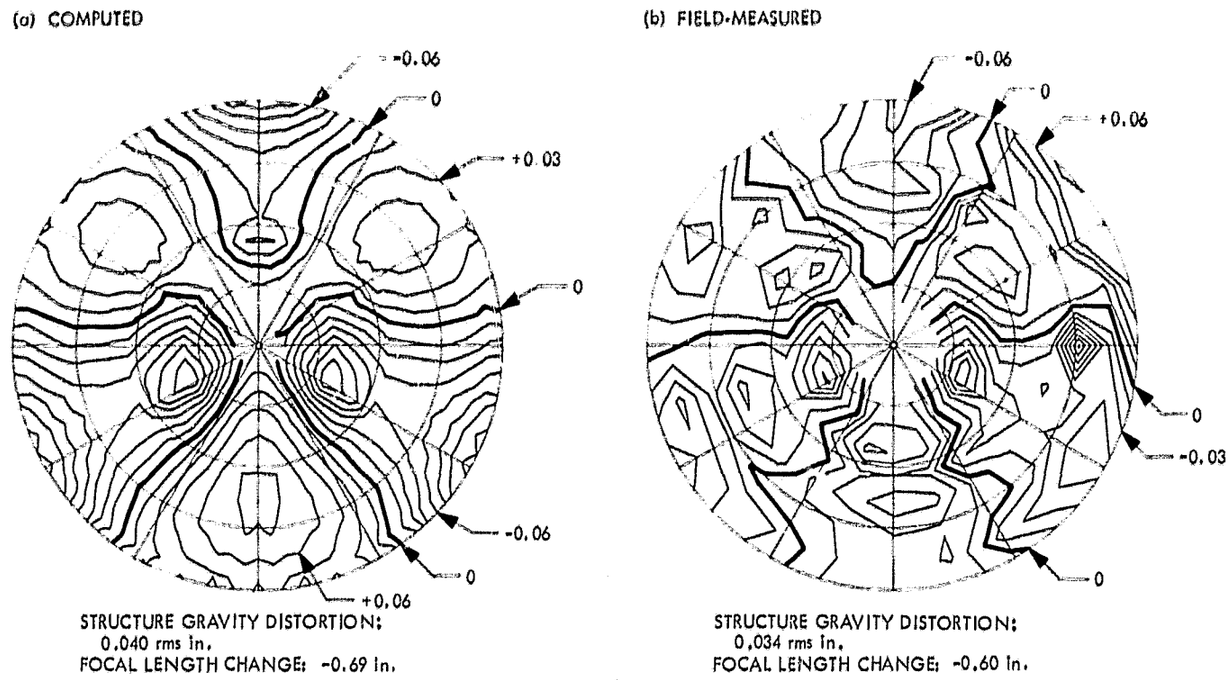


**Fig. 8. Horizon attitude contour maps of one-half RF-pathlength distortions**

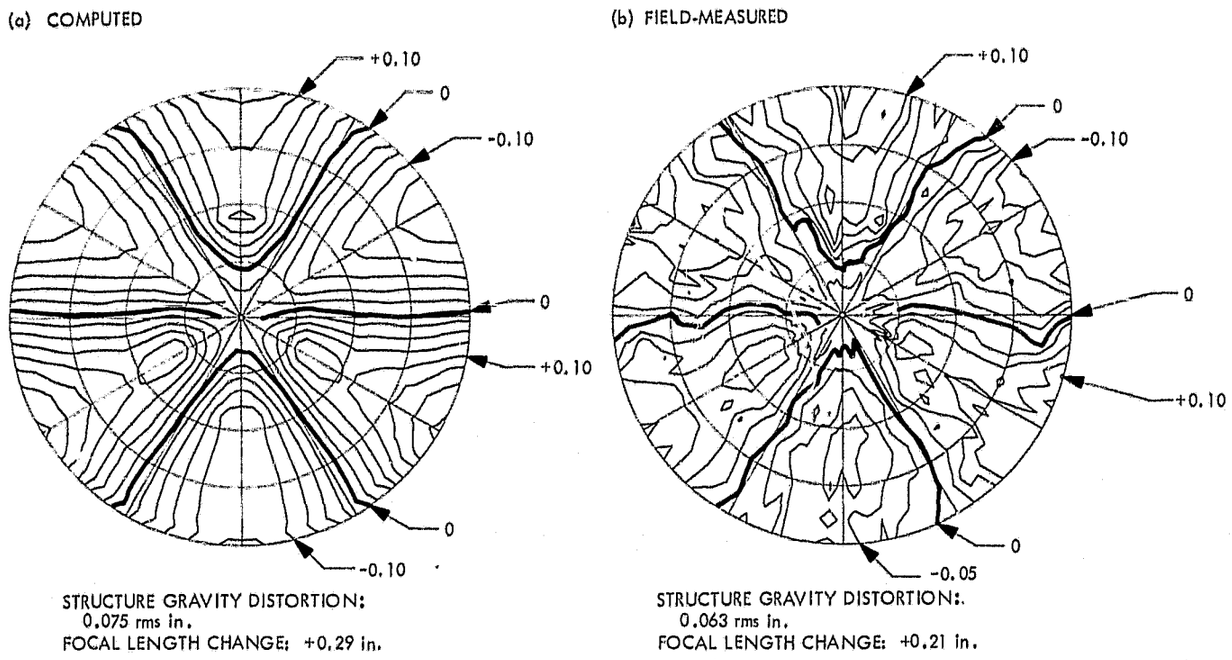


**Fig. 9. Zenith attitude contour maps of one-half RF-pathlength distortions**

AAS is exactly symmetric in halves. In computing, quadrant symmetry was a necessary assumption. Analysis of a half-structure may produce closer agreement between computations and field-measured data.

In summary, the predicted AAS surface tolerance is considered well defined, since the independent analytic results and the field measurements are in close agreement.

### C. Predicted Overall System Efficiency and Gain

By considering the computed RF optics efficiency (Section II-A), the computed rms surface tolerance (Section II-B), and Fig. 7, we can arrive at a predicted overall system efficiency and gain. The results, based on an acceptance of the axial focusing effort (which was shown to be worthwhile), are given in Table 7. Note that this

**Table 7. Computed system efficiency and gain**

| Elevation angle, deg | Surface tolerance, rms in. | Surface tolerance efficiency, % | Overall system efficiency, % | System gain, dB |
|---|---|---|---|---|
| 0 | 0.065 | 70.6 | 44.4 | 71.5 |
| 15 | 0.058 | 76.4 | 48.0 | 71.9 |
| 30 | 0.051 | 81.4 | 51.2 | 72.2 |
| 45 | 0.048 | 83.2 | 52.3 | 72.3 |
| 60 | 0.055 | 78.6 | 49.5 | 72.0 |
| 75 | 0.075 | 64.4 | 40.5 | 71.1 |
| 90 | 0.102 | 43.5 | 27.4 | 69.4 |

table includes the effect of a nearly 0.2-dB dissipation loss within the XCE feedcone.

## III. Measured Performance of the AAS: X-Band

### A. Source Selection and Feed Performance

The XCE feedcone used for previous 85-ft-antenna evaluation was transferred to the AAS without change. Figure 10 shows the feed installed (February 1–5, 1968). As described in Ref. 5, this listen-only feed system was designed as a low-noise total power radiometer for observing a few radioastronomical sources. In all cases the system was sensitive to right-hand circular polarization. Three nonthermal sources, 3C123, 3C274, and 3C405, were selected as primary calibrators as well as the planet Venus—assumed to exhibit a brightness temperature of 600°K. Also, 3C273 was included as a useful point source. Table 8 lists the sources, assumed sizes and distributions, beam correction factors, and antenna temperatures accepted for a 100-percent-efficient 210-ft-diameter antenna operated at 8448 MHz. Table 8 also gives a derived flux for the variable 3C273 that is based on temperature measurements made during focusing tests. In Table 8 it is clear that Cygnus A subtends nearly the expected half-power beamwidth of the system. For this reason the beam correction factor is large (nearly −2 dB) and therefore not highly reliable under conditions of possible beamwidth changes with elevation angle. Cygnus A was retained, however, because of previous observation as an 85-ft-antenna calibrator at the same wavelength with the same feed (Ref. 5).

Operating in a ground checkout mode the XCE feedcone, pointing to the zenith, exhibits a 33.5°K total operating temperature. The individual noise sources are thought to be $T_M$ = 13.7°K at the maser input, $T_L$ = 13.2°K, $T_F$ = 0.1°K at the maser input, and $T_A$ = 6.8°K at the horn aperture where $T_M$, $T_L$, $T_F$, and $T_A$ are the maser, the loss, the followup receiver, and the antenna temperature contributions, respectively. When the feedcone is operated on the AAS, an additional 3.3°K noise temperature at zenith is observed. This additional

**Table 8. Source characteristics at 8448 MHz (Epoch 1968.1)**

| Characteristic | Source | | | |
|---|---|---|---|---|
| | 3C123 | 3C273 | 3C274 | 3C405 |
| Type | 2-dimensional gaussian | Quasar | 1-dimensional gaussian | 2 points |
| Size, arc-s | 20 | Point | 1 × 45 | 116-arc-s separation |
| 8448-MHz flux $S$, W/m² • Hz | $9.4 \times 10^{-26}$ | $42.5 \times 10^{-26}$ (variable) | $42 \times 10^{-26}$ | $187.6 \times 10^{-26}$ |
| Spectral index | −0.86 | — | −1.02 halo<br>−0.44 core | −1.2 |
| [a]Beam correction $C_s$ | 1.021 | 1.000 | 1.055 | 1.56 |
| [b]Antenna temperature $T_A$ 100%, °K | 10.7 | 49.5 | 46.4 | 140.1 |

[a]137-arc-s half-power beamwidth selected.
[b]$T_A$ 100% = 1.1655 $S/C_s$, S × $10^{26}$.

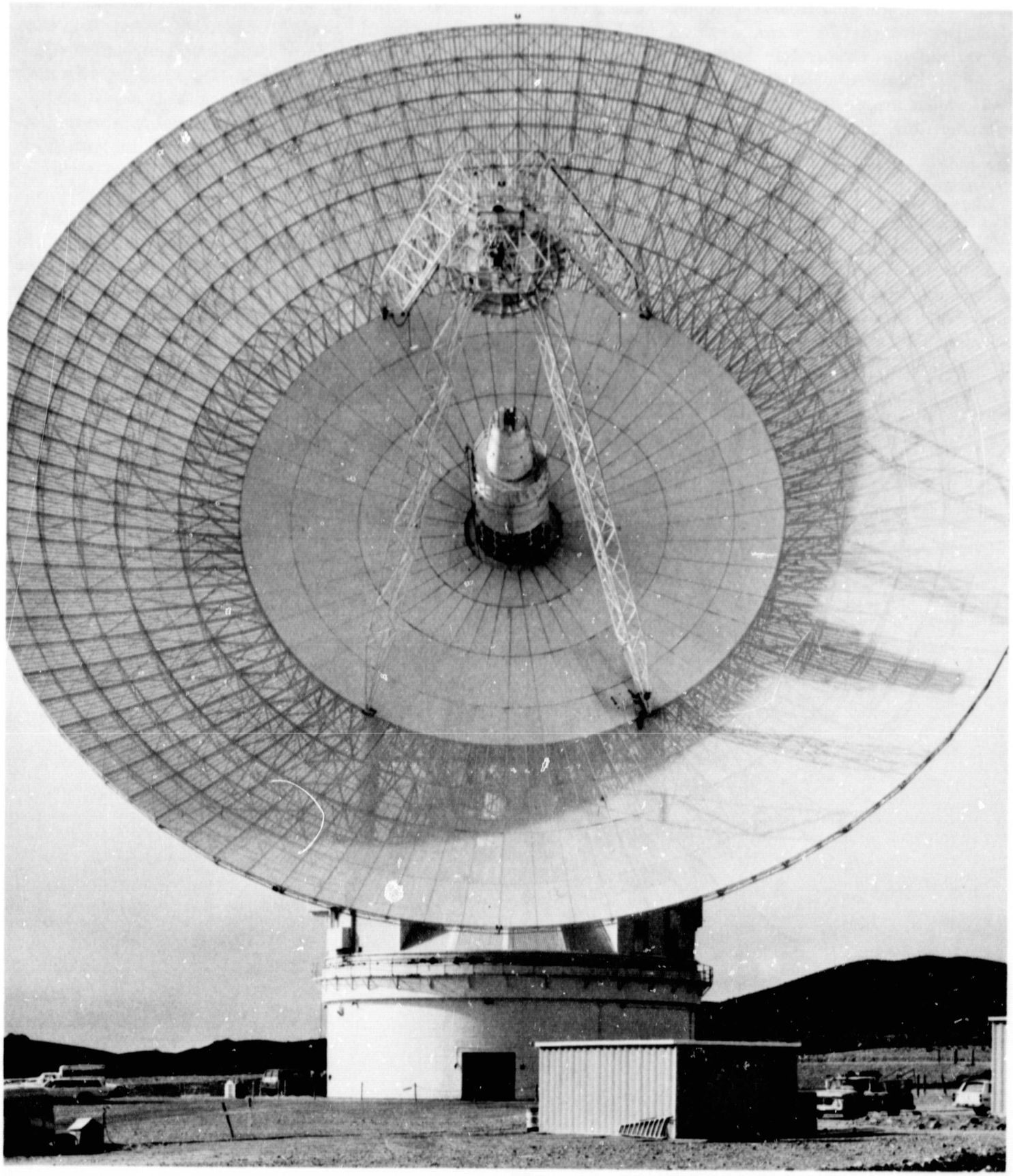

Fig. 10. Advanced antenna system with XCE feedcone installed

noise is caused primarily from feed spillover and quadripod scatter towards the warm earth. A total X-band cassegrain antenna temperature defined at the horn aperture of 10.1°K appears a reasonable estimate. Comparable S-band values are an incremental 3.6°K and a total of 9.3°K (Ref. 13).

### B. Focusing

The AAS is equipped with subreflector axial drives and, as described earlier, structural calculations indicated that a worthwhile improvement in effective surface tolerance was available by use of this adjustment. Focusing was the first step taken in the X-band evaluation. The receive-system noise temperature with 3C273 in the beam was maximized. Figure 11 shows the RF results for the source both ascending and descending in elevation angle, a step considered essential because of previous long time constant hysteresis in focal length found on an 85-ft structure (Ref. 5). Also shown in Fig. 11 is a single verification of focus at a high elevation angle and the structural predictions based on Table 5. The structural data were best-fitted to the RF results; again, as was so with 85-ft reflector evaluations, a maximum signal focus occurs at X-band approximately 0.8 in. above the S-band focus. That is, the control room synchro-indication at S-band at a 45-deg elevation angle is approximately 0.1 in. in Fig. 11. Although not verified, this antenna-independent effect is believed caused by the best-fitting, achieved by means of signal-peaking, to the phasefront seen in the scattered patterns (Figs. 3 and 4). In these figures, the distortion occurring near the rim of the paraboloid is caused

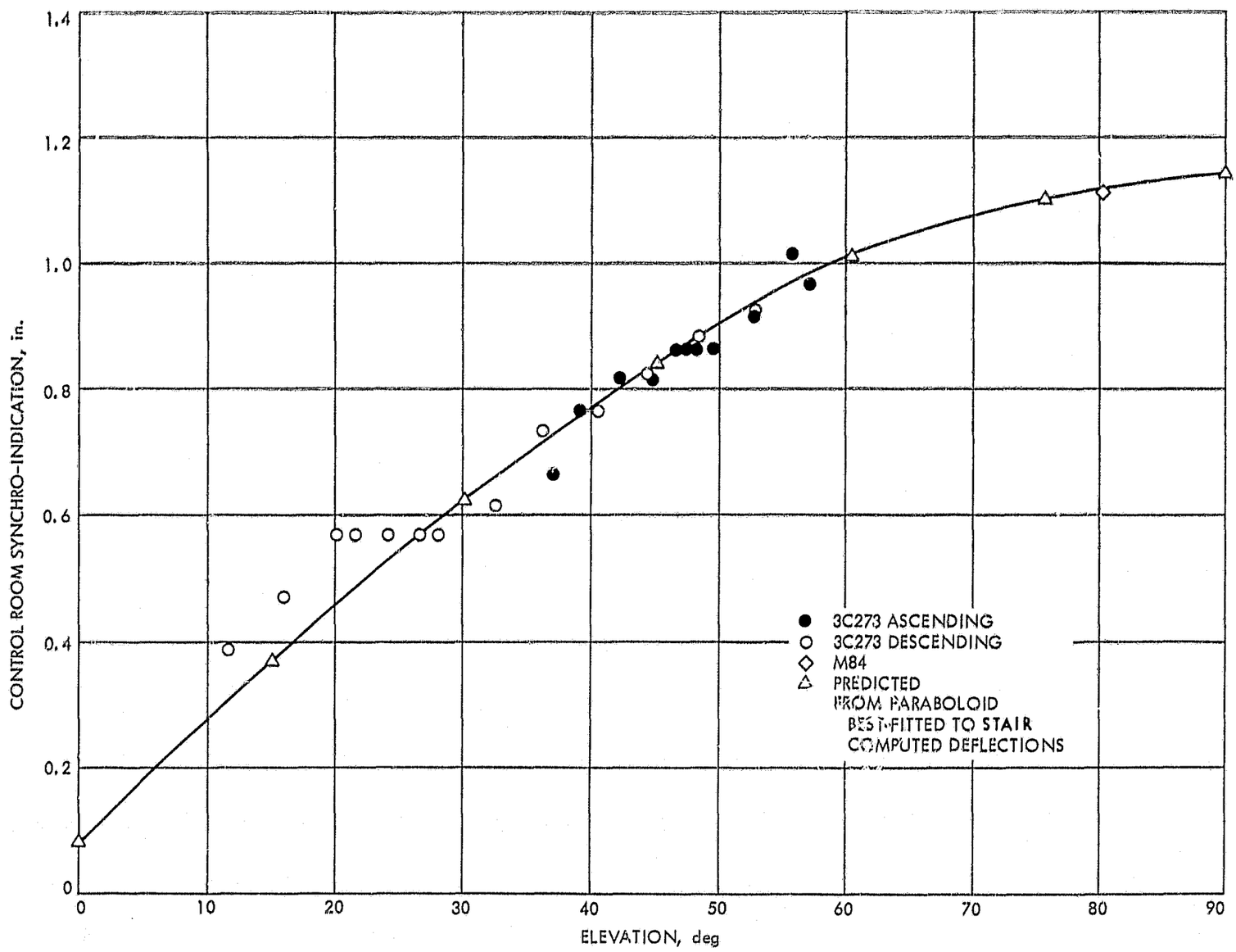


**Fig. 11. Focus as a function of elevation angle**

by the oversized beam shaping flange attached to the hyperboloid.

Once found repeatable and in agreement with structural predictions, the focus data in Fig. 11 were used throughout the X-band evaluation in a manual correction mode, with focus trimming with elevation angle in approximately 0.050-in. steps being used.

### C. Radiometric Technique: System Efficiency Measurements

The technique used to determine the change in system temperature due to the source (referenced to the maser input flange) was as follows:

(1) Update, if necessary, the focal adjustment setting according to Fig. 11 verified predictions.

(2) Boresight the antenna by the half-power-points method.

(3) Obtain five Y-factors between the antenna and ambient termination.

(4) Steer off source 1 deg in azimuth if below 45-deg elevation, 1 deg in elevation if above 45-deg elevation.

(5) Obtain five Y-factors between the antenna and ambient termination.

(6) Repeat steps (3) through (5) three additional times, alternating the direction of the off-source steering.

Figure 12 shows a sample of the data recording form used. The form requires one-half to one hour to complete. Figure 13 shows a sample of machine-reduced data and gives the difference between total operating temperatures on-source and off-source, which is attributed to the source flux.

The technique of the previous paragraph was found adequate above approximately a 20-deg elevation angle. Below that, the ephemeris command, operating without *a priori* correction terms, was inadequate for good pointing, i.e., boresight updating more frequent than one-half to one hour was found necessary. The brief test period

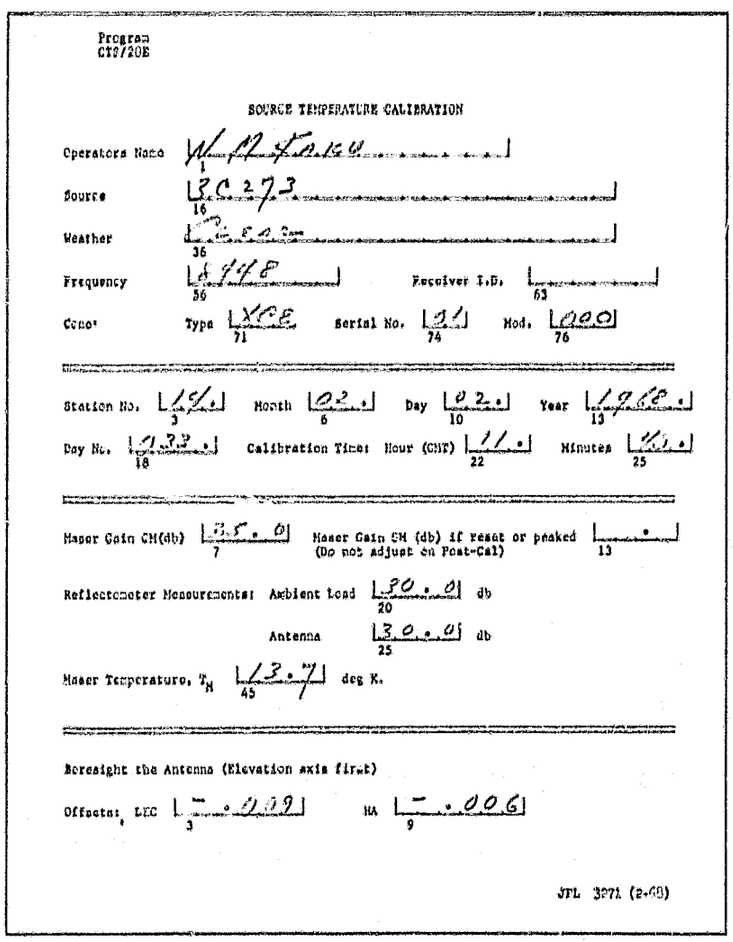

Program
CT3/20E

SOURCE TEMPERATURE CALIBRATION

Operators Name [illegible]

Source 3C273

Weather [illegible]

Frequency 8448 Receiver I.D. [blank]

Cone: Type XCE Serial No. 01 Mod. 000

Station No. 14. Month 02. Day 02. Year 1968.

Day No. 033. Calibration Time: Hour (GMT) 11. Minutes 40.

Maser Gain CH(db) 35.0 Maser Gain CH (db) if reset or peaked (Do not Adjust on Post-Cal) .

Reflectometer Measurements: Ambient Load 30.01 db

Antenna 30.01 db

Maser Temperature, $T_N$ 13.7 deg K.

Boresight the Antenna (Elevation axis first)

Offsets: XEC -.009 EL -.006

JPL 3071 (2-68)

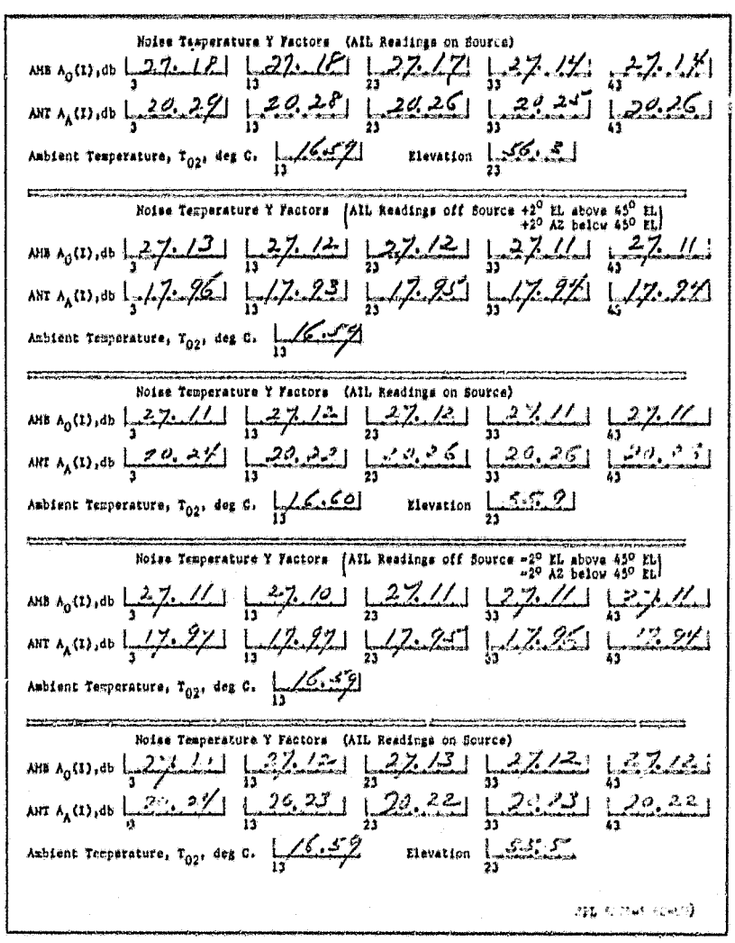

Noise Temperature Y Factors (All Readings on Source)

AMB $A_0(I)$,db 27.18 27.18 27.17 27.14 27.14

ANT $A_A(I)$,db 20.29 20.28 20.26 20.25 20.26

Ambient Temperature, $T_{02}$, deg C. 16.57 Elevation 56.5

Noise Temperature Y Factors (All Readings off Source +2° EL above 45° EL, +2° AZ below 45° EL)

AMB $A_0(I)$,db 27.13 27.12 27.12 27.11 27.11

ANT $A_A(I)$,db 17.96 17.93 17.95 17.94 17.94

Ambient Temperature, $T_{02}$, deg C. 16.57

Noise Temperature Y Factors (All Readings on Source)

AMB $A_0(I)$,db 27.11 27.12 27.12 27.11 27.11

ANT $A_A(I)$,db 20.24 20.23 20.26 20.26 20.25

Ambient Temperature, $T_{02}$, deg C. 16.60 Elevation 56.9

Noise Temperature Y Factors (All Readings off Source -2° EL above 45° EL, -2° AZ below 45° EL)

AMB $A_0(I)$,db 27.11 27.10 27.11 27.11 27.11

ANT $A_A(I)$,db 17.94 17.93 17.95 17.95 17.94

Ambient Temperature, $T_{02}$, deg C. 16.59

Noise Temperature Y Factors (All Readings on Source)

AMB $A_0(I)$,db 27.11 27.12 27.13 27.12 27.12

ANT $A_A(I)$,db 20.24 20.23 20.22 20.23 20.22

Ambient Temperature, $T_{02}$, deg C. 16.59 Elevation 56.5

Fig. 12. Sample data recording form

available precluded an adequate definition and automation of *a priori* correction terms.

From Table 8 and the radiometric technique, the overall system efficiency at the maser input flange is obtained (Fig. 14). No atmospheric corrections are included; the concept adopted here is to accept the atmosphere as a system loss, as would be observed during a deep space tracking mission. Although the weakest of the three calibrators, 3C123 was given priority because of a superior source distribution. Figure 14 shows good consistency among the three nonthermal sources, and is in good agreement with overall efficiency predictions.

The planet Venus, a low elevation angle source, was observed, although with some scatter (Fig. 15). The mean value of 2.4°K at the maser reference flange at 25-deg elevation angle is consistent with the nonthermal sources, indicating the assumed 600°K blackbody was not in serious error. The planet Jupiter, subtending approximately 44 arc-s compared with the 137-arc-s beamwidth, produced a temperature increase of 9.3°K at 45-deg elevation, again referenced to the maser input flange.

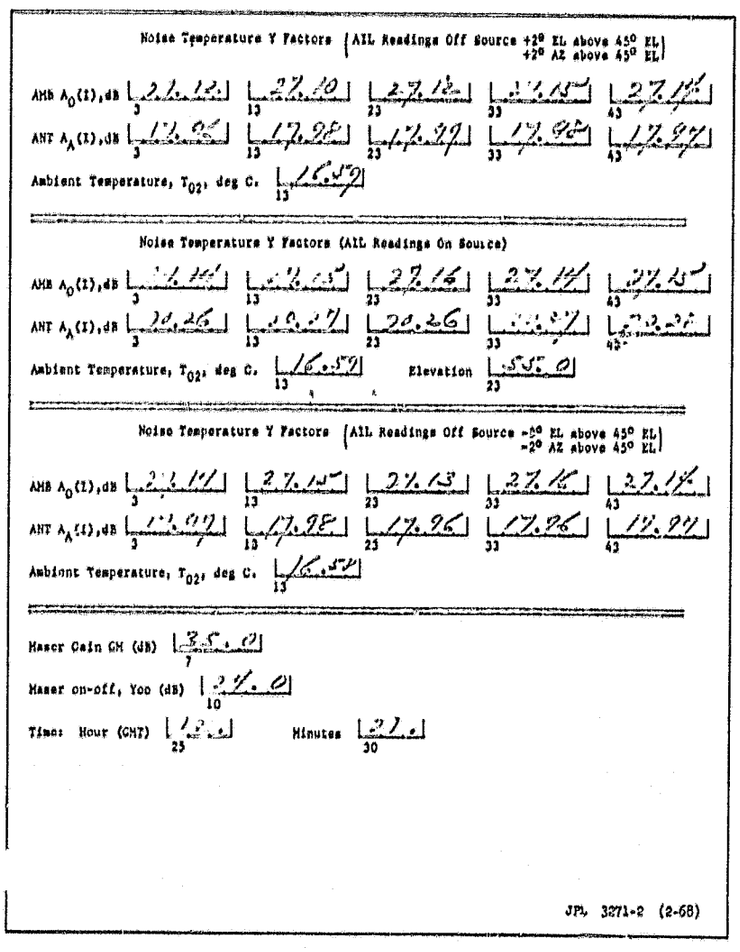


Fig. 12 (contd)

```
SOURCE NO.62 TEMPERATURE PROGRAM GTS/DSN
STATION NO. 14
OPERATOR N M MAKU
SOURCE 3C273
DATE  2/ 9/1968   DAY NO.  33
TIME(GMT) 11 HOURS 48 MINUTES
FREQUENCY(MC) 8448
WEATHER CLEAR

RECEIVER
OFFSET(DEG.) DELAZ   =0.000  DELEL  =0.000
MASER GAIN(DB) 35.0
PEAKED MASER GAIN(DB)
REFL.MEAS.(DB) AMB,LOAD 30.0  ANT, 30.0
MASER ON-OFF(DB) 24.0
MASER TEMP.(DEG.K) 13.7

  ON SOURCE   AMB. TEMP, 16.59    OFF SOURCE   AMB. TEMP, 16.59  SOURCE TEMP,
AO(I)   AA(I)   YOA(I)  TSAON(I)  AO(I)   AA(I)   YOA(I)  TSAOFF(I)  TS(I)
27.18   28.29    6.89    62.39    27.13   17.96    9.17    36.88     25.47
27.18   28.28    6.90    62.28    27.12   17.95    9.19    36.71     25.49
27.17   28.26    6.91    62.26    27.10   17.95    9.17    36.88     25.18
27.14   28.25    6.89    62.35    27.11   17.94    9.17    36.88     25.47
27.14   28.26    6.88    62.49    27.11   17.94    9.17    36.88     25.61

TSAON      62.29,DEG.K        TSAOFF      36.85,DEG.K        TS    25.44,DEG.K
TR         14.91,DEG.K        TR          14.91,DEG.K        PETS   0.12,DEG.K
TF          1.21,DEG.K        TF           1.21,DEG.K
PETSA(M,I)  0.11,DEG.K        PETSA(M,I)   0.06,DEG.K
PETSA(M)    0.85,DEG.K        PETSA(M)     0.82,DEG.K
PETSA       0.41,DEG.K        PETSA        0.30,DEG.K        EL    56.30,DEG

  ON SOURCE   AMB. TEMP, 16.68    OFF SOURCE   AMB. TEMP, 16.59  SOURCE TEMP,
AO(I)   AA(I)   YOA(I)  TSAON(I)  AO(I)   AA(I)   YOA(I)  TSAOFF(I)  TS(I)
27.11   28.24    6.87    62.64    27.11   17.97    9.14    37.14     25.50
27.12   28.22    6.98    62.21    27.10   17.97    9.13    37.22     24.98
27.12   28.26    6.86    62.78    27.11   17.95    9.16    36.97     25.81
27.11   28.24    6.85    62.93    27.11   17.96    9.15    37.05     25.87
27.11   28.24    6.85    62.93    27.11   17.94    9.17    36.80     26.04

TSAON      62.76,DEG.K        TSAOFF      37.05,DEG.K        TS    25.64,DEG.K
TR         14.91,DEG.K        TR          14.91,DEG.K        PETS   0.15,DEG.K
TF          1.21,DEG.K        TF           1.21,DEG.K
PETSA(M,I)  0.20,DEG.K        PETSA(M,I)   0.09,DEG.K
PETSA(M)    0.89,DEG.K        PETSA(M)     0.84,DEG.K
PETSA       0.42,DEG.K        PETSA        0.31,DEG.K        EL    55.98,DEG

  ON SOURCE   AMB. TEMP, 16.59    OFF SOURCE   AMB. TEMP, 16.59  SOURCE TEMP,
AO(I)   AA(I)   YOA(I)  TSAON(I)  AO(I)   AA(I)   YOA(I)  TSAOFF(I)  TS(I)
27.18   28.24    6.86    62.78    27.12   17.96    9.16    36.97     25.81
27.12   28.23    6.89    62.35    27.10   17.98    9.12    37.31     25.04
27.13   28.22    6.91    62.06    27.12   17.99    9.13    37.22     24.84
27.12   28.23    6.89    62.35    27.15   17.98    9.17    36.88     25.47
27.12   28.22    6.90    62.20    27.14   17.97    9.17    36.88     25.32

TSAON      62.35,DEG.K        TSAOFF      37.05,DEG.K        TS    25.29,DEG.K
TR         14.91,DEG.K        TR          14.91,DEG.K        PETS   0.15,DEG.K
TF          1.21,DEG.K        TF           1.21,DEG.K
PETSA(M,I)  0.18,DEG.K        PETSA(M,I)   0.14,DEG.K
PETSA(M)    0.83,DEG.K        PETSA(M)     0.86,DEG.K
PETSA       0.42,DEG.K        PETSA        0.31,DEG.K        EL    55.58,DEG

  ON SOURCE   AMB. TEMP, 16.59    OFF SOURCE   AMB. TEMP, 16.58  SOURCE TEMP,
AO(I)   AA(I)   YOA(I)  TSAON(I)  AO(I)   AA(I)   YOA(I)  TSAOFF(I)  TS(I)
27.14   28.26    6.88    62.49    27.14   17.97    9.17    36.88     25.61
27.15   28.27    6.88    62.49    27.15   17.98    9.17    36.88     25.61
27.16   28.26    6.98    62.28    27.13   17.96    9.17    36.88     25.32
27.14   28.27    6.87    62.64    27.16   17.96    9.28    36.63     26.01
27.15   28.28    6.87    62.64    27.14   17.97    9.17    36.88     25.75

TSAON      62.49,DEG.K        TSAOFF      36.83,DEG.K        TS    25.66,DEG.K
TR         14.91,DEG.K        TR          14.91,DEG.K        PETS   0.12,DEG.K
TF          1.21,DEG.K        TF           1.21,DEG.K
PETSA(M,I)  0.12,DEG.K        PETSA(M,I)   0.08,DEG.K
PETSA(M)    0.85,DEG.K        PETSA(M)     0.83,DEG.K
PETSA       0.41,DEG.K        PETSA        0.30,DEG.K        EL    55.68,DEG

        SUMMARY

TSAON      62.46,DEG.K        TSAOFF      36.95,DEG.K        TS    25.51,DEG.K
TR         14.91,DEG.K        TR          14.91,DEG.K        PETS   0.12,DEG.K
TF          1.21,DEG.K        TF           1.21,DEG.K
PETSA(M,I)  0.18,DEG.K        PETSA(M,I)   0.11,DEG.K
PETSA(M)    0.84,DEG.K        PETSA(M)     0.83,DEG.K
PETSA       0.41,DEG.K        PETSA        0.30,DEG.K        EL    55.67,DEG
ERR CRDS
```

Fig. 13. Sample machine-reduced data

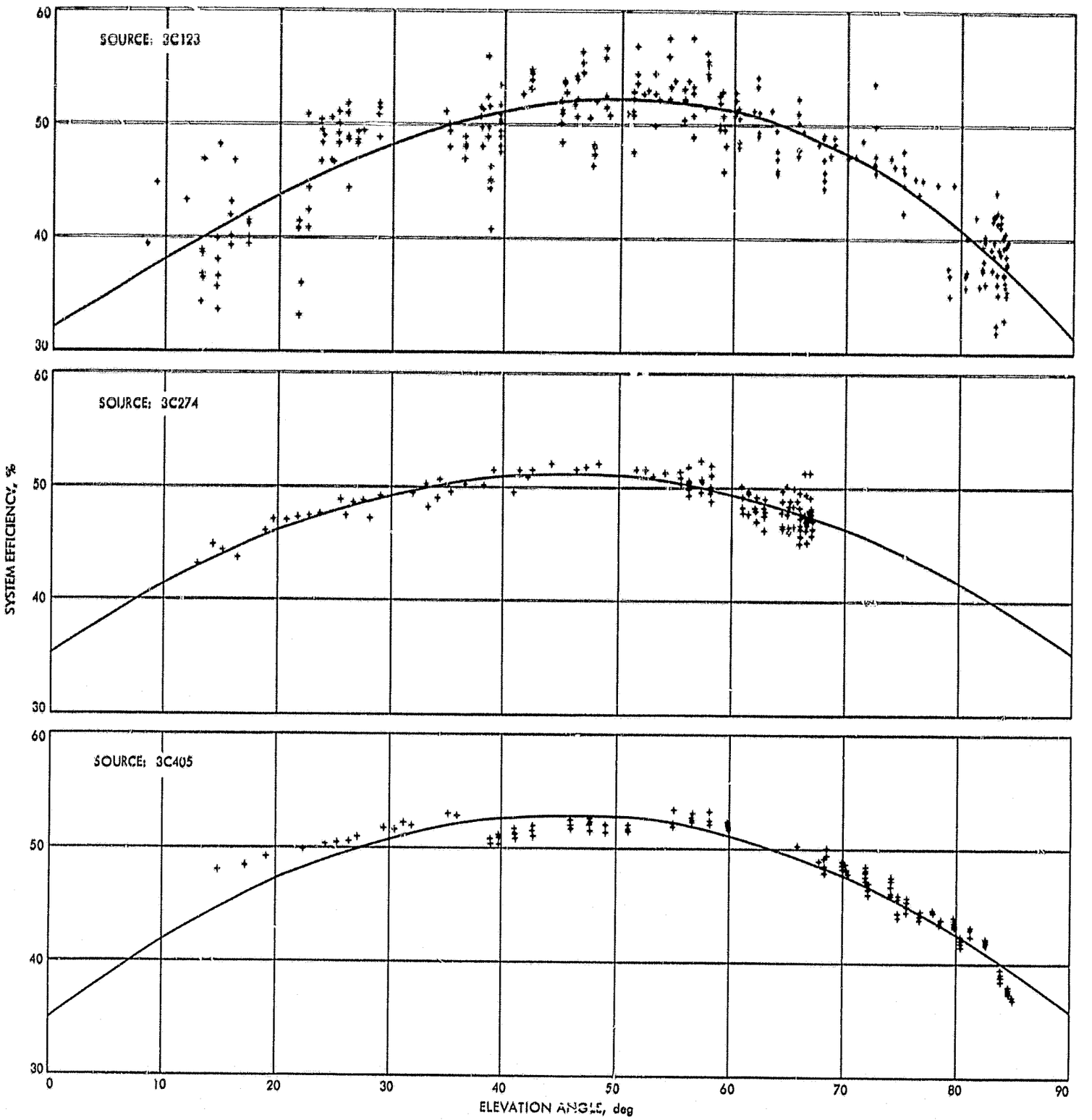


**Fig. 14. System efficiency as a function of elevation angle**

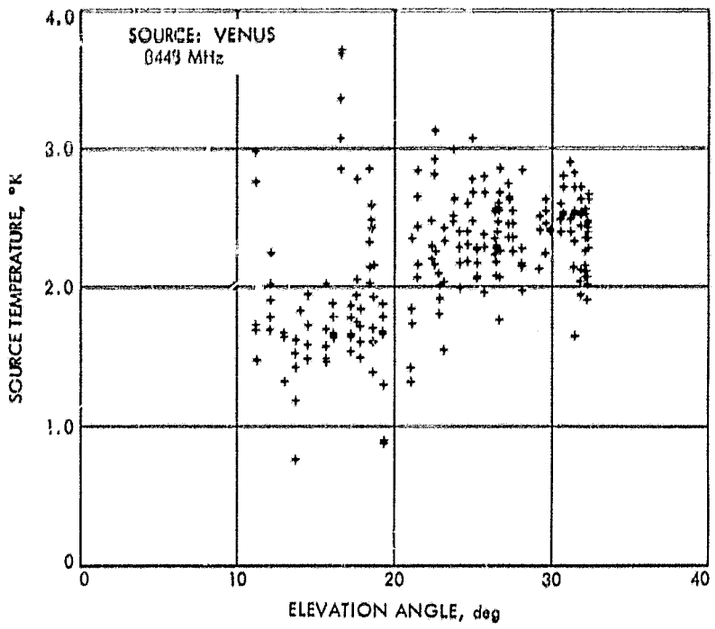


**Fig. 15. Source temperature as a function of elevation angle**

### D. Surface Tolerance and Total Operating Temperature

The surface tolerance of the reflecting system may be obtained from the computed RF optics efficiency data and the measured 3C123 efficiency data. Because the gain loss from surface tolerance was expected to range approximately 1–3 dB, a determination of surface tolerance by means of the computed RF optics efficiency is considered a useful and accurate method. Figure 16 gives the mean and standard deviation limits for the rms surface tolerance as determined from the radio measurements. The standard deviation limits include only the measurement scatter. Figure 16 includes the structurally predicted rms surface tolerance for the axial-focused condition from Section II-B. To obtain the radio data in this instance the contribution of atmospheric loss must be considered. This was done by accepting the common flat earth secant law, applicable above an elevation angle of about 10 deg, and by selecting a theoretical 0.036-dB atmospheric loss at zenith.

As Fig. 16 shows, the radio measurements indicate a better surface tolerance than that predicted when at zenith, essentially in agreement with field-measured structural data (Table 6). The radio-observed surface tolerance near horizon appears somewhat worse than expected in Fig. 16. This is a sensitive function of the selected zenith loss, however, and a fitted value of 0.055 dB at zenith with the secant dependence will force perfect agreement between predicted and radio-measured rms at a 10-deg elevation angle.

Zenith losses of 0.055 and 0.036 dB were further investigated with the aid of total operating temperature measurements as a function of elevation angle. Figure 17 shows the temperature measurements with both zenith constants included, for an assumed effective physical temperature of the atmosphere of 290°K. The higher zenith loss appears to provide a good fit, leaving open the question of effective physical temperature of the atmosphere. With the use of an improved density-weighted average for the physical temperature, the 0.060-dB zenith loss and 260°K yield the same results.

It should be concluded that the zenith attenuation experienced approximates 0.06 dB and the surface tolerance over all elevation angles is essentially that calculated by structural means, with evidence that the field-measured structural data more accurately describes the reflector system when oriented to the zenith.

### E. Drift Curves

Drift curves of the quasar 3C273 at a 35-deg elevation angle (Fig. 18) confirm the expected 0.038-deg half-power beamwidths. Scans of the double Cygnus (Fig. 19) in hour angle and declination show the expected beam broadening in hour angle, which is nearly the major axis of the source. A single scan of the sun (Fig. 20) reveals sharp edges and well-resolved fine structure. Dual scans of the moon were made (Fig. 21) to eliminate the possibility of a radiometer gain drift. The limbs appear very sharp, with the eastern region noticeably cooler.

### F. Pointing

Throughout the tests, the precision I mode was used to point the AAS. In this mode the main reflector structure is optically coupled to the relatively small master equatorial mirror which, in turn, is precision-positioned by the computer. An example of the overall RF precision afforded in this mode is shown in Fig. 22, which is a radiometer recording obtained during RF boresighting on Cygnus A. With a previously determined −0.006 deg declination offset, the approximate half-power points are determined as +0.017 and −0.025 deg in declination, the mean of which is taken as an update to a −0.004 deg offset. Figure 22 continues the bracketing procedure in the hour angle axis where the extended source requires greater offsets for a half-power indication. Again, a change of 1 or 2 mdeg is discerned as accomplished in a stable manner.

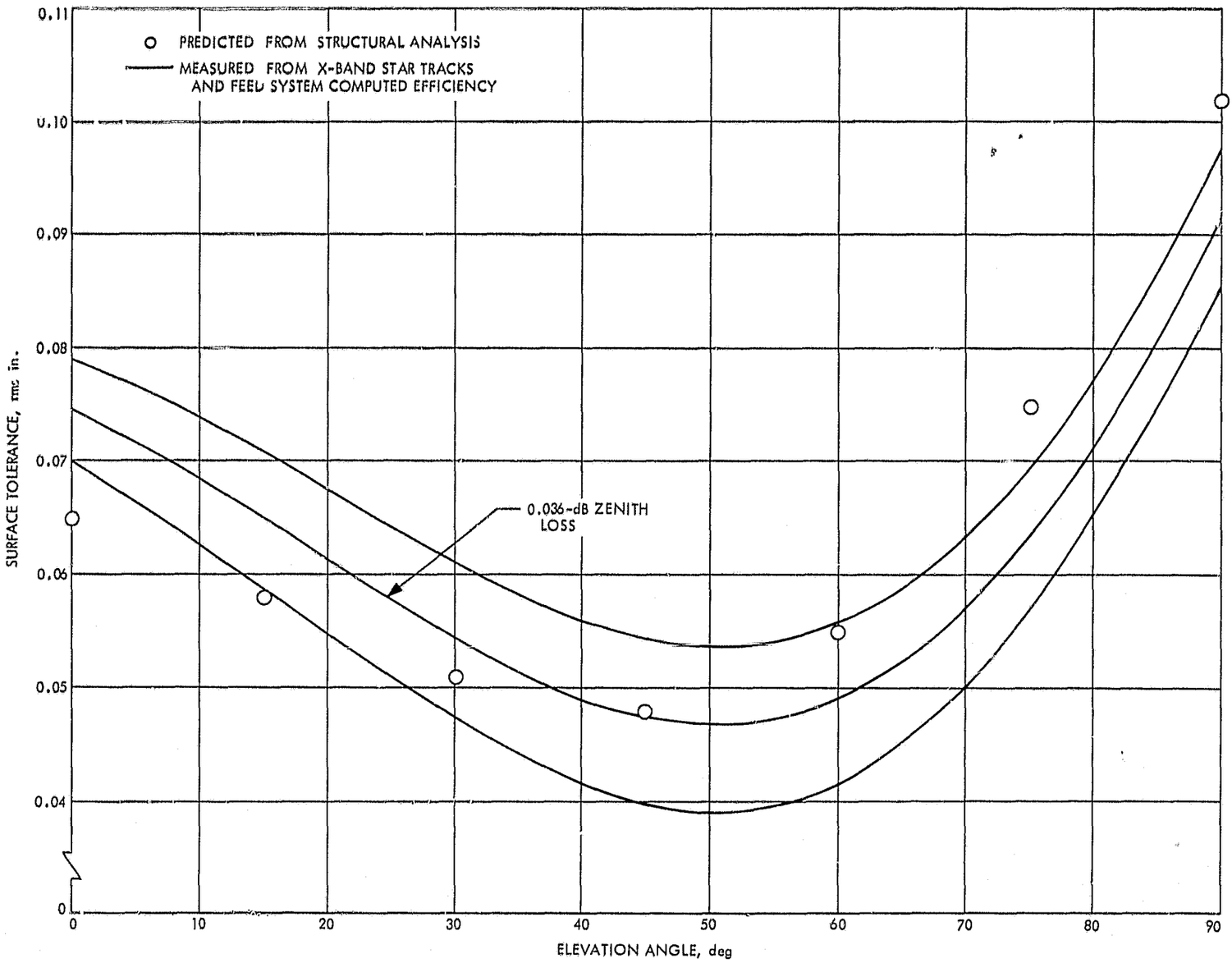


**Fig. 16. Root-mean-square surface tolerance as a function of elevation angle**

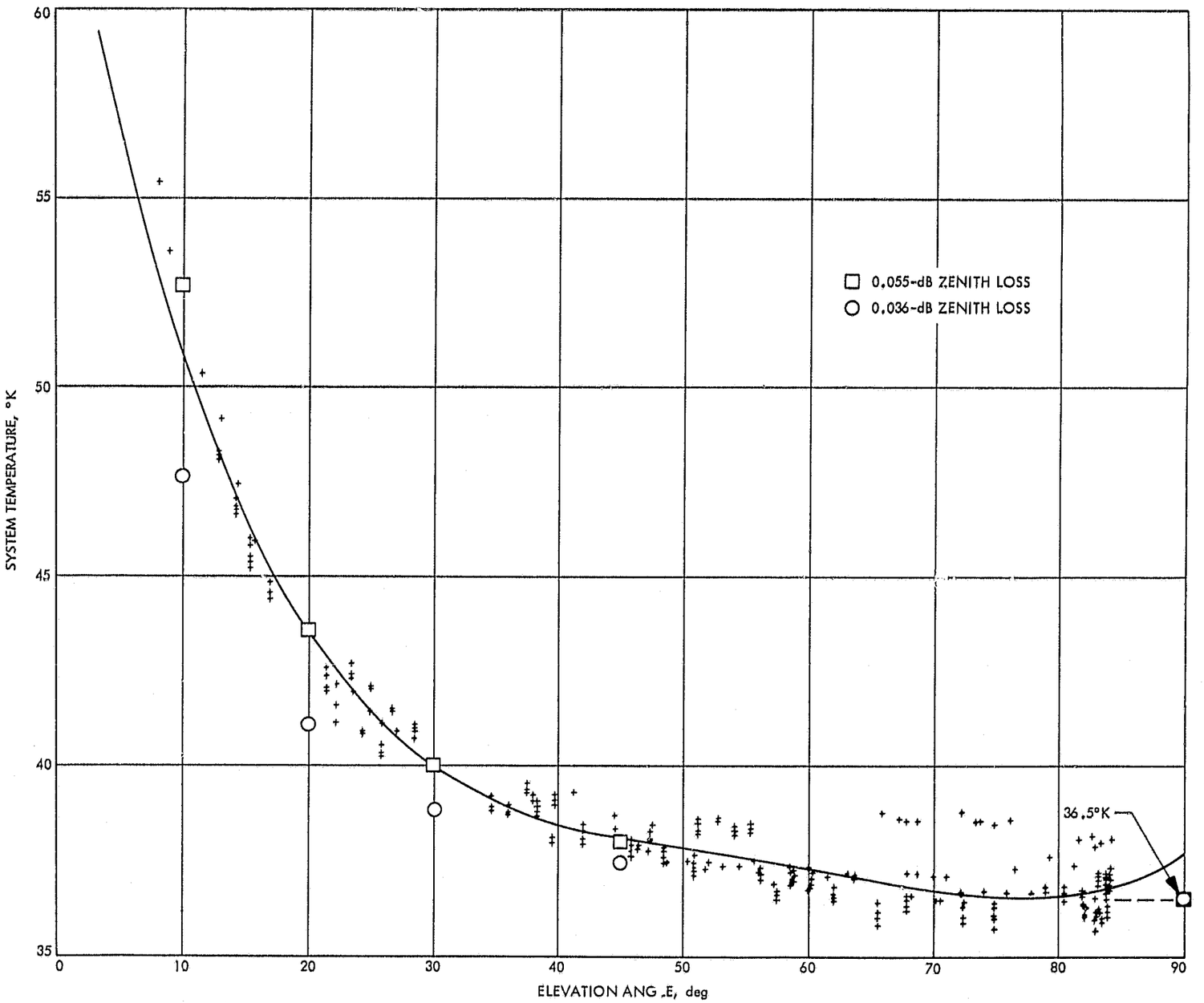


**Fig. 17. Total system operating temperature as a function of elevation angle**

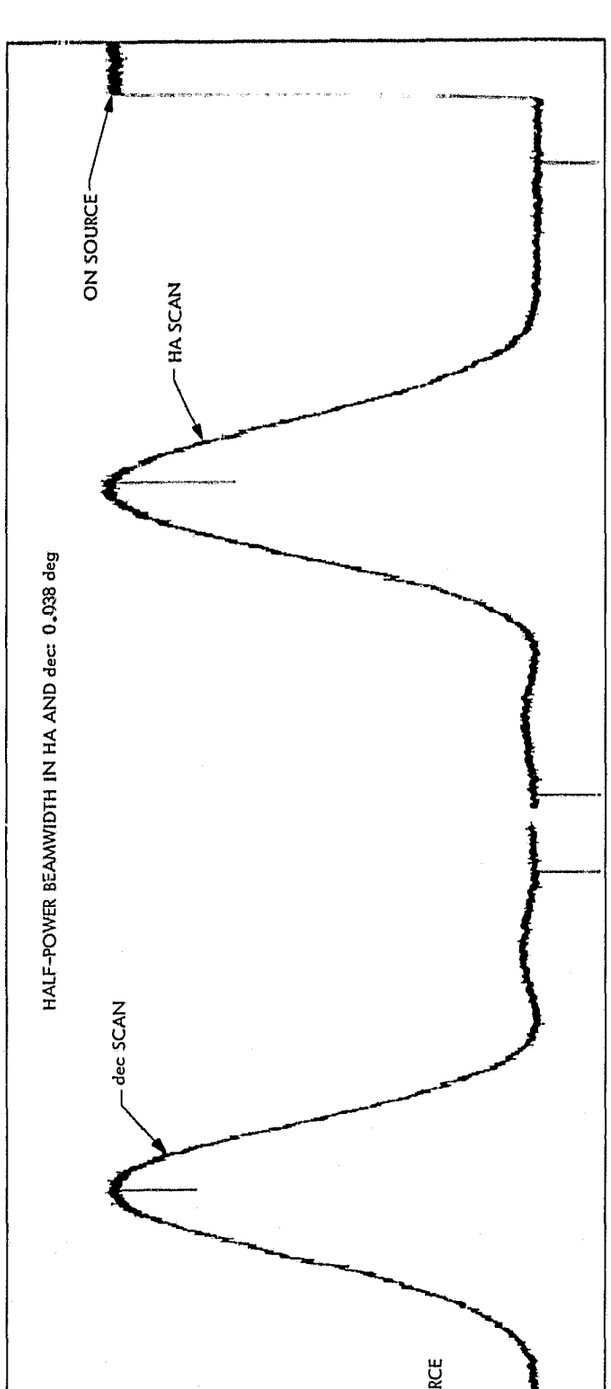


**Fig. 18. Scan of 3C273 at 35-deg elevation**

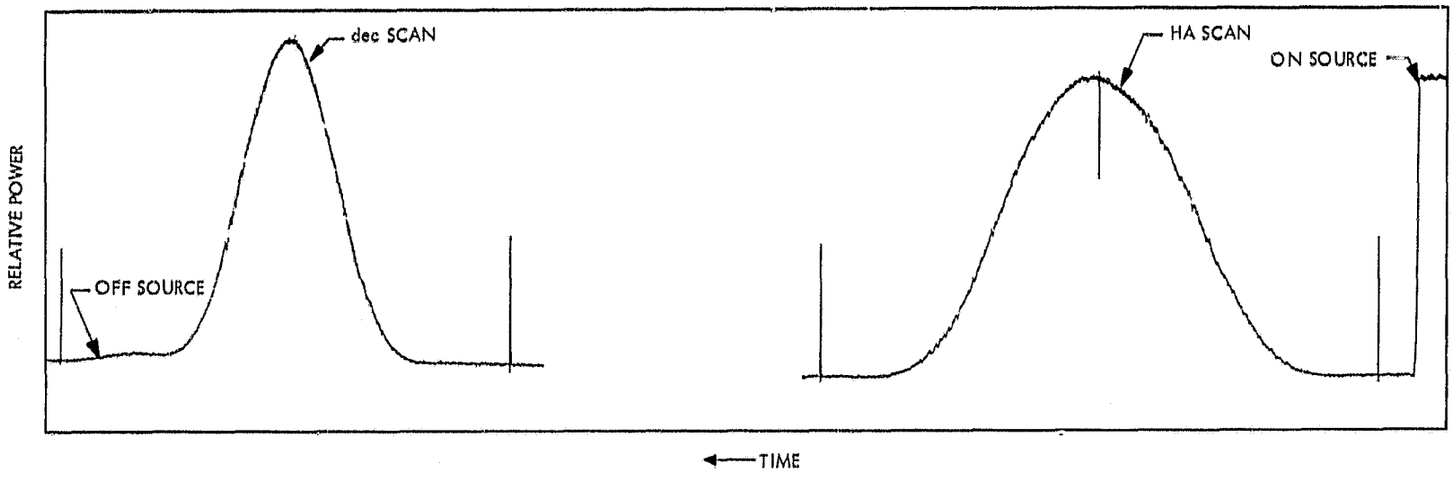


**Fig. 19. Scans of 3C405**

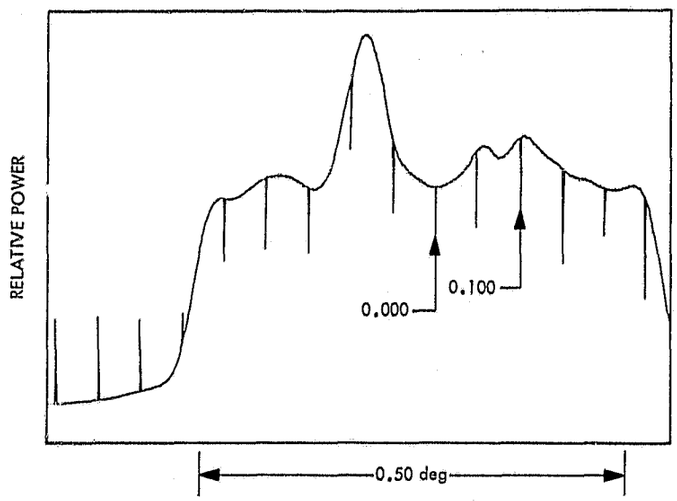


**Fig. 20. Scan of sun**

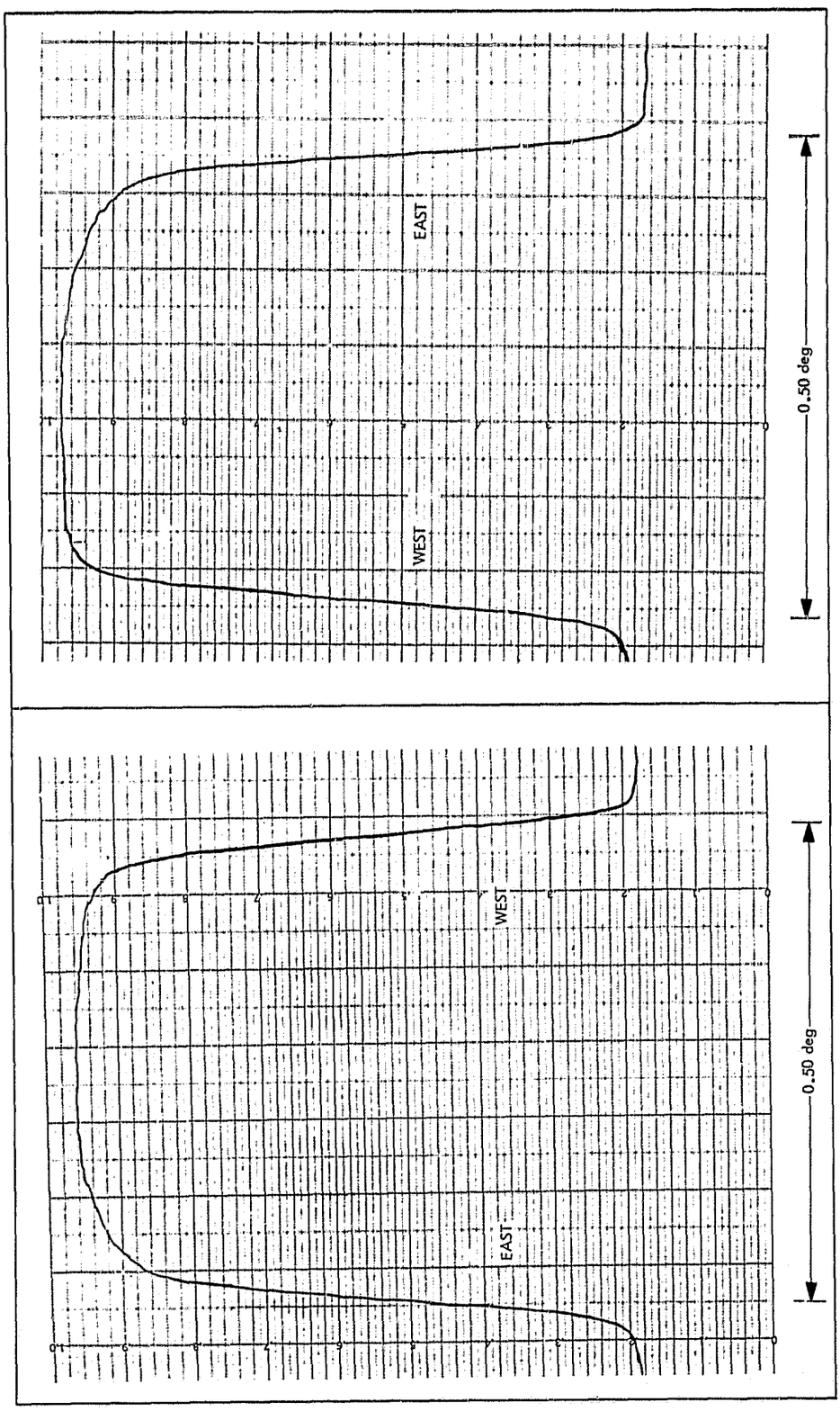


**Fig. 21. Scans of moon**

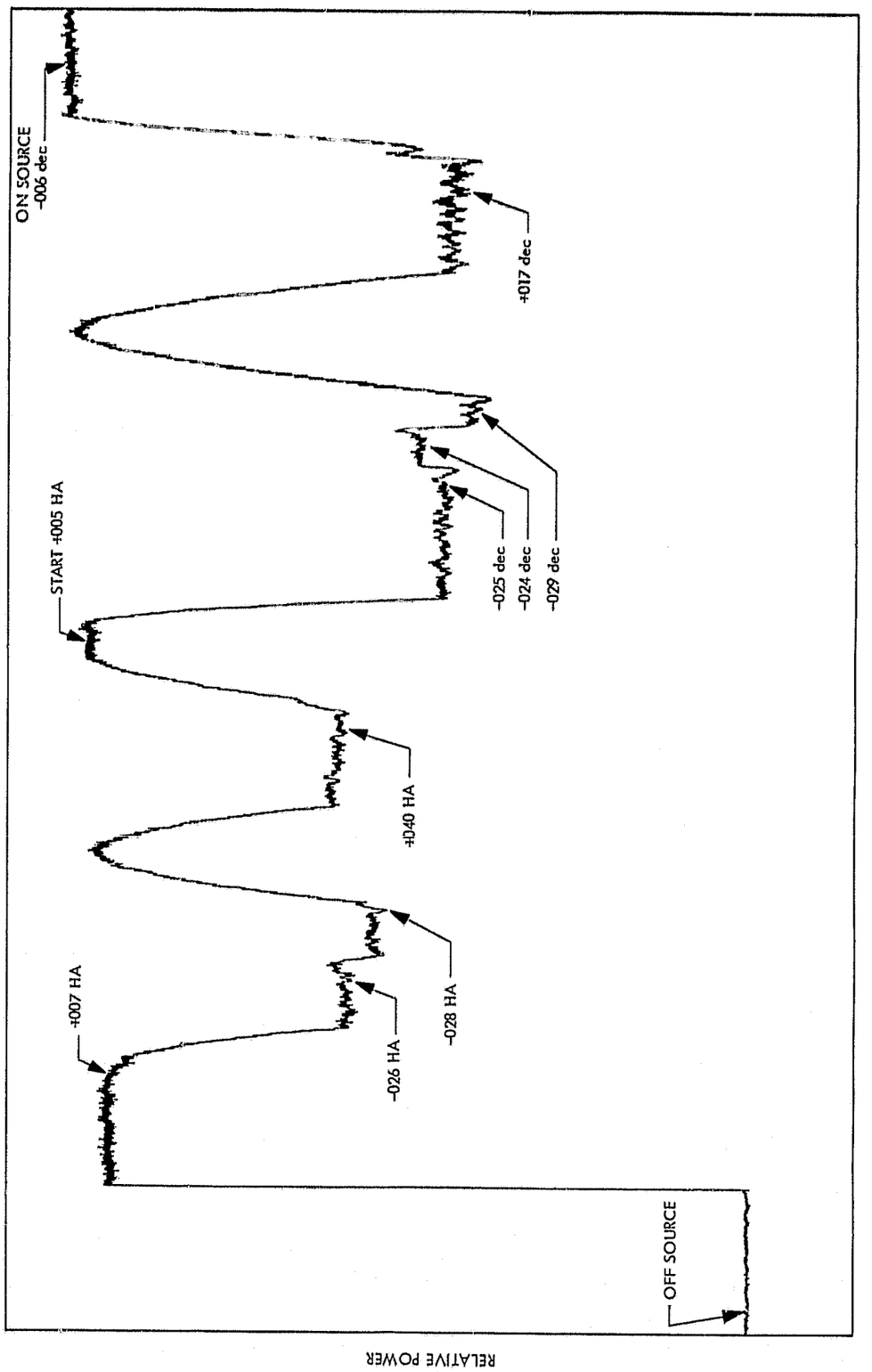


**Fig. 22. Cygnus boresighting recording**

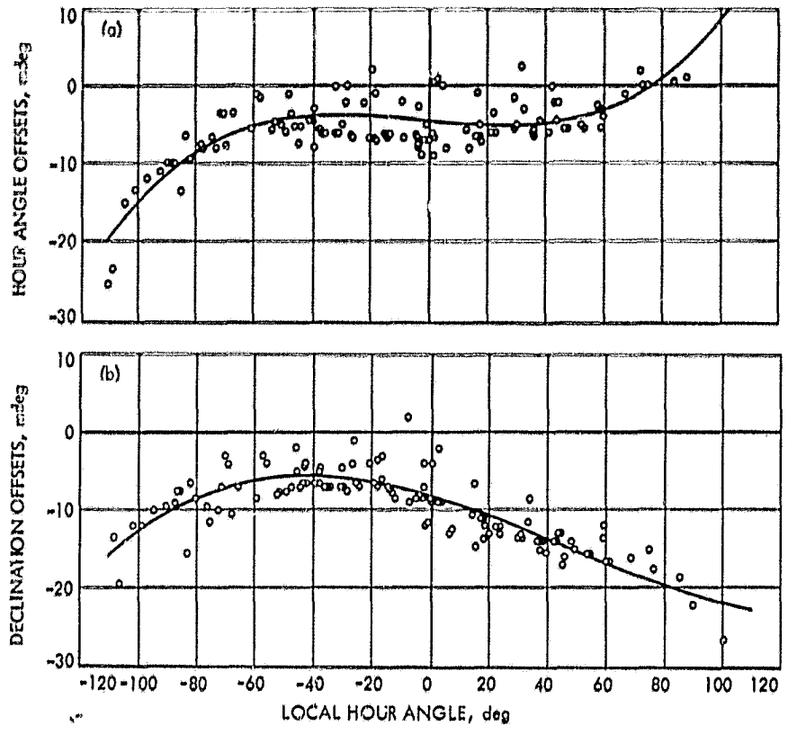


**Fig. 23. Angle offsets as a function of local hour angle**

Figure 23 considers absolute accuracy of the pointing system. In the absence of a thorough study of source position accuracy, the best available data were used in an ephemeris program and accepted as absolute (Table 9). As described in detail elsewhere (Ref. 14), the AAS tipping structure is a carefully pointing-compensated system; that is, various structural gravity deflections are opposed, resulting in unusually low overall RF boresight errors as a function of elevation angle.* As Fig. 23 shows, in the absence of *a priori* corrections (the brief test period was inadequate to well define and automate corrections as noted earlier), the absolute pointing, for the 4 sources spanning declinations of +2 to +40 deg, may be specified as approximately 1 minute, peak, with the exception of very low elevation angles. Therefore, acquiring a known astronomical object within the X-band half-power beamwidth (38 mdeg) without resort to any correction terms seems probable.

Figure 23 includes third-order curves fitted on the basis of least squares. The standard deviation, $\sigma$, is 2.4 mdeg in declination and 2.5 mdeg in hour angle. It therefore appears probable that a known astronomical object may be acquired within a tenth of the X-band half-power beamwidth, using the corrections generated. Note that this performance applies for sources within declinations +2 to +40 deg, based on a 5-day sample.

*Originally, the repeatable errors were to be removed with an elevation angle driven cam modulating the intermediate reference surface. To date, this refinement has not been considered necessary, and has therefore not been made.

**Table 9. Source positions**

| Source | Declination | Right ascension | 1968 date |
|---|---|---|---|
| 3C123 | 29°36′37.0″ | $04^h35^m03^s.9$ | Feb 5 |
| 3C273 | 02°13′44.0″ | $12^h27^m29^s.0$ | Feb 2 |
| 3C274 | 12°34′01.7″ | $12^h29^m12^s.6$ | Feb 3 |
| 3C405 | 40°40′24.7″ | $19^h58^m22^s.0$ | Feb 4 |

## IV. Conclusions

In a brief RF test program at X-band, 8448 MHz, conducted on the Goldstone 210-ft-diameter advanced antenna system in February 1968, 24-h/day radio star tracking shows that the peak system gain and efficiency observed are 72.3 dB and 52%, respectively. The accuracy of radio star calibrations of this kind is considered ±0.8 dB, with high confidence. Ordered changes due to gravity loading in the surface tolerance and focal length occurred as predicted by analytic structural models. The combined accuracy of the master equatorial pointing and reflector boresight systems was found adequate for X-band, assuming that observed systematic effects are

removed. The precision of the pointing system and the repeatability of the total structure appear compatible; furthermore the system gain is as expected.

Generally good weather was experienced during the tests, with little or no occurrence of winds in excess of 20 MPH. The days were quite sunny; normal thermal effects were apparently encountered. Some performance estimates with thermal and wind loading on the AAS are available (Ref. 15). The generally dry climate at the Goldstone complex allowed a total operating noise temperature of the system of less than 37°K at zenith.

If we accept a surface tolerance maximum of 0.065 rms in. as applicable over a wide range of elevation angles, gain limit should occur in the 2-cm band. Although further experience at X-band using this instrument is needed, a significant ground capability for weather-dependent space communications or radio or radar astronomy is available at X-band.

## References


1. Levy, G. S., et al., "Lunar Range Radiation Patterns of a 210-ft Antenna at S-Band," *IEEE Trans. Ant. Prop.*, Vol. AP-15, No. 2, pp. 311–313, March 1967.
2. Levy, G. S., Bathker, D. A., and Ludwig, A. C., "Gain Measurements of the Advanced Antenna System Using *Surveyor I* Signals," in *The Deep Space Network*, Space Programs Summary 37-44, Vol. III, pp. 100–105. Jet Propulsion Laboratory, Pasadena, Calif., Mar. 31, 1967.
3. Goldstein, R. M., et al., *The Superior Conjunction of Mariner IV*, Technical Report 32-1092, Jet Propulsion Laboratory, Pasadena, Calif., Apr. 1, 1967.
4. Stelzried, C. T., and Otoshi, T. Y., "RF Techniques," in *The Deep Space Network*, Space Programs Summary 37-39, Vol. III, pp. 86–100. Jet Propulsion Laboratory, Pasadena, Calif., May 31, 1966.
5. Bathker, D. A., *Radio-Frequency Performance of an 85-ft Ground Antenna: X-Band*, Technical Report 32-1300. Jet Propulsion Laboratory, Pasadena, Calif., July 1, 1968.
6. Rusch, W. V. T., *Scattering of a Spherical Wave by an Arbitrary Truncated Surface of Revolution*, Technical Report 32-434. Jet Propulsion Laboratory, Pasadena, Calif., May 1963.
7. Ludwig, A. C., "Antenna Feed Efficiency," in *Supporting Research and Advanced Development*, Space Programs Summary 37-26, Vol. IV, pp. 200–208. Jet Propulsion Laboratory, Pasadena, Calif., Apr. 30, 1964.
8. Katow, M. S., "Primary Reflector Analysis (210-ft-diam Antenna)," in *The Deep Space Network*, Space Programs Summary 37-52, Vol. II, pp. 86–92. Jet Propulsion Laboratory, Pasadena, Calif., July 31, 1968.
9. Katow, M. S., and Schmele, L. W., "Antenna Structures: Evaluation Techniques of Reflector Distortions," in *Supporting Research and Advanced Development*, Space Programs Summary 37-40, Vol. IV, pp. 176–184. Jet Propulsion Laboratory, Pasadena, Calif., Aug. 31, 1966.
10. Silver, S., *Microwave Antenna Theory and Design*, p. 173. McGraw-Hill Book Co., Inc., New York, 1949.

## References (contd)


11. Bathker, D. A., "Radiation Pattern Programs," in *Computer Programs for Antenna Feed System Design and Analysis: Volume I. Programs and Sample Cases*, p. 107. Edited by A. C. Ludwig. Technical Report 32-979. Jet Propulsion Laboratory, Pasadena, Calif., Apr. 15, 1967.

12. Ruze, J., "Antenna Tolerance Theory—A Review," *Proceedings IEEE*, Vol. 54, No. 4, pp. 633–640, April 1966.

13. Levy, G. S., et al., "The Ultracone: An Ultra-Low-Noise Space Communication Ground Radio Frequency System," *IEEE Trans. Microwave Theory Techniques*, Vol. MTT-16, No. 9, pp. 596–602, September 1968.

14. Katow, M. S., "210-ft-Antenna Quadripod Structural Analysis, II," in *The Deep Space Network*, Space Programs Summary 37-53, Vol. II, pp. 73–76. Jet Propulsion Laboratory, Pasadena, Calif., Sept. 30, 1968.

15. Katow, M. S., "210-ft Antenna Primary Reflector Structure Distortions Due To Thermal Differences and Wind Loadings," in *The Deep Space Network*, Space Programs Summary 37-54, Vol. II, pp. 56–58. Jet Propulsion Laboratory, Pasadena, Calif., Nov. 30, 1968.

_____, "Techniques Used To Evaluate the Performance of the NASA/JPL 210-Foot Reflector Structure Under Environmental Loads," in *Structures Technology for Large Radio and Radar Telescope Systems*. Edited by J. W. Mar and H. Liebowitz. The M.I.T. Press, Cambridge, Massachusetts and London, 1969.





NASA — JPL — Coml., L.A., Calif.